

# **Q-factor measurement of on-chip microdisk optical resonators**

Master's Thesis submitted

to

**Prof. Dr. Arno Rauschenbeutel**

Humboldt-Universität zu Berlin

Mathematisch-Naturwissenschaftliche Fakultät

Institut für Physik

Optical Science

by

**Wanrong Li**

(531805)

Examiners: **Prof. Dr. Arno Rauschenbeutel**

**Prof. Dr. Oliver Benson**

Supervisors: **Prof. Dr. Arno Rauschenbeutel**

**Dr. Sofia Pazzagli**

Submitted in partial fulfillment of the requirements

for the degree of

**Master of Science**

Berlin, August 22, 2022



## Acknowledgements

First, I would like to sincerely thank Prof. Dr. Arno Rauschenbeutel for allowing me to work on this project under his supervision during my time in his group. I would want to especially express my gratitude to Dr. Sofia Pazzagli, who was always there whenever I had questions concerning my research or writing. This thesis would not have been completed without her assistance and guidance and enormous patience in every step throughout the process. I would also like to thank Thomas Hoinkes for fabricating the optical nanofibers and all of the group members for their generous help. In order to preliminarily check the quality of the fabricated resonators, a scanning electron microscopy (SEM) imaging process is performed in the group of Dr. Katja Höflich (Helmholtz-Zentrum Berlin), I would like to appreciate Dr. Höflich for her support.

I would also like to acknowledge Prof. Dr. Oliver Benson as the second reviewer of this thesis.

This thesis is based on a collaboration with Ferdinand-Braun-Institut (FBH). I would like to thank Dr. Andreas Thies and Jan Schlegel for their assistance with the fabrication of chips.

Finally, I take this opportunity to thank my family for their support and encouragement throughout my years of study.



# Abstract

Dielectric microdisk resonators are a type of optical whispering gallery mode (WGM) resonators in which the light field is confined near the circumference of the structure via continuous total internal reflection. In this thesis, the quality factor (Q-factor) measurement of on-chip silica microdisk resonators is demonstrated.

Chapter 1 provides an introduction to whispering gallery mode resonators. Several parameters to describe the performance of optical resonators are then presented, followed by the coupling model used in this thesis for Q-factor measurement in which an optical nanofiber is used for light coupling.

In Chapter 2, the on-chip microdisk resonators studied in this thesis are introduced. The resonators are made of silicon dioxide (silica) and they are grown on silicon wafers. This chapter presents a description of the fabrication process, followed by a morphological study, the mode analysis of the fabricated microdisks, and a pre-analysis of Q-factor.

In Chapter 3, the optical and mechanical setup established for the Q-factor measurement in the frequency domain are described, together with a detailed analysis of the mode propagation in optical nanofiber.

In Chapter 4, the performance of the experimental setup is at first evaluated using a bottle microresonator. Then, the Q-factor of 200  $\mu\text{m}$  diameter microdisks with different thicknesses (i.e. different numbers of supported modes) are measured, and intrinsic Q-factor on the order of  $10^6$  are obtained.

In Chapter 5, the main conclusions of the thesis are summarised, and possible improvements of this experiment are discussed.

# Contents

<b>Introduction</b>	<b>1</b>
<b>1 Fundamentals of whispering gallery mode microresonators</b>	<b>2</b>
1.1 Parameters of optical WGM resonators . . . . .	2
1.2 Total internal reflection and evanescent field . . . . .	5
1.3 Light coupling methods . . . . .	7
<b>2 Silica on silicon microdisk resonators</b>	<b>13</b>
2.1 Fabrication and morphological characterization of on-chip microdisk resonator . . . . .	13
2.2 Mode analysis of microdisk resonators . . . . .	16
2.3 Preliminary consideration of Q-factor . . . . .	20
<b>3 Experimental method for Q-factor measurement</b>	<b>22</b>
3.1 Optomechanical setup . . . . .	22
3.2 Optical nanofiber . . . . .	26
3.3 Sample layout . . . . .	32
<b>4 Results and discussion</b>	<b>35</b>
4.1 A bottle resonator as a reference sample . . . . .	35
4.2 Q-factor measurement of microdisk resonators . . . . .	37
<b>5 Summary and outlook</b>	<b>46</b>
<b>References</b>	<b>48</b>



# Introduction

Whispering gallery mode (WGM) microresonators have been of great interest due to their compact sizes and their very high quality factors (Q-factor). They have been used in many fields of research, such as sensor technologies [1–4], narrow linewidth laser module [5, 6], light switches and filters for optical communication [7, 8], cavity quantum electrodynamics [9], the frequency comb generation [10] in the high precision spectroscopy [11, 12]. All these applications rely on the spatial and temporal confinement of light by the microresonator [13], among which the Q-factor describes the temporal confinement properties. Several examples of different WGM resonators are the microspheres, microtoroids, microdisks, microrings, and bottle resonators, all of which have cylindrical symmetry as their common geometry. Among different WGM resonators, this thesis focuses on the on-chip silica microdisk resonators. Monolithically integrated systems with microdisk resonators offer a unique potential for sensor technologies, such as temperature sensors [14, 15] and bio-sensors [16] that can benefit from such systems.

By continuous total internal reflection (TIR), the circular symmetry defines the path for the light propagating in dielectric resonators near the curved boundaries [17]. These are the so-called whispering gallery modes (WGMs). During the TIR process from the curved surfaces of the resonator, evanescent fields of WGMs occur in the region between the boundaries of the resonator and the caustic points [18]. These evanescent fields can thus be used for light coupling in (and out) to (from) the resonators with the help of evanescent couplers such as an optical nanofiber used in this thesis work. And the coupling efficiency is modified by the overlap of the evanescent fields of the two components. In other words, by changing the relative distance between the nanofiber and the resonator.

In this thesis, Q-factor measurement in the frequency domain is achieved by measuring the power transmitted through the nanofiber to obtain the resonance linewidth  $\Delta\nu$  of the resonator. And  $\Delta\nu$  can be used for the calculation of the intrinsic Q-factor according to its definition.

# 1 Fundamentals of whispering gallery mode microresonators

## 1.1 Parameters of optical WGM resonators

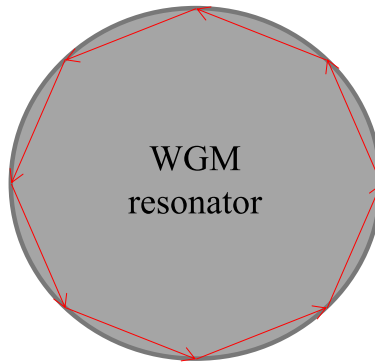


Figure 1: WGMs in a ray optics description.

The first description of the whispering gallery waves phenomenon was made by Lord Rayleigh and discovered for sound waves traveling along the circular dome of St Paul's Cathedral in London [19]. A whisper could be passed from one person to another in the interior of a whispering gallery if both persons were close enough to the wall. Similarly, dielectric structures with circular symmetry allow electromagnetic waves to propagate along the circumference in a way of the so-called whispering gallery modes (WGMs). WGMs are commonly imagined as closed-trajectory rays confined by the continuous total internal reflection from the curved surface of the resonator [20], as illustrated in Figure 1.

In a WGM resonator with a radius  $R$ , a circulating light with wavelength  $\lambda \ll R$  can constructively interfere when after a round trip it returns in phase, i.e. with a phase shift equal to an integer  $l$  multiple of  $2\pi$ . This condition is fulfilled only for distinct wave numbers  $k = 2\pi/\lambda$  and at resonance, the light intensity inside the optical resonator reaches a peak value due to constructive interference. The resonance condition can be expressed as [21]:

$$2\pi nR \approx l\lambda \tag{1.1}$$

where  $n$  is the refractive index of the resonator material. This equation describes that in order to have constructive interference, the multiple wavelengths should be approximately the circumference of the resonator.

In Figure 2, the calculated transmission spectrum of a general waveguide coupled with a WGM resonator is plotted. The spectrum with respect to frequency is a set of equally spaced dips and the frequency spacing between two consecutive resonance dips  $\nu_i$  and  $\nu_{i+1}$  is called the free spectral range (FSR)  $\Delta\nu_{FSR}$ :

$$\Delta\nu_{FSR} = \nu_{i+1} - \nu_i = \frac{c}{n2\pi R} \quad (1.2)$$

FSR is size-dependent and for microresonators with smaller diameters, the resonance frequencies are more sparsely distributed throughout the spectrum [22].

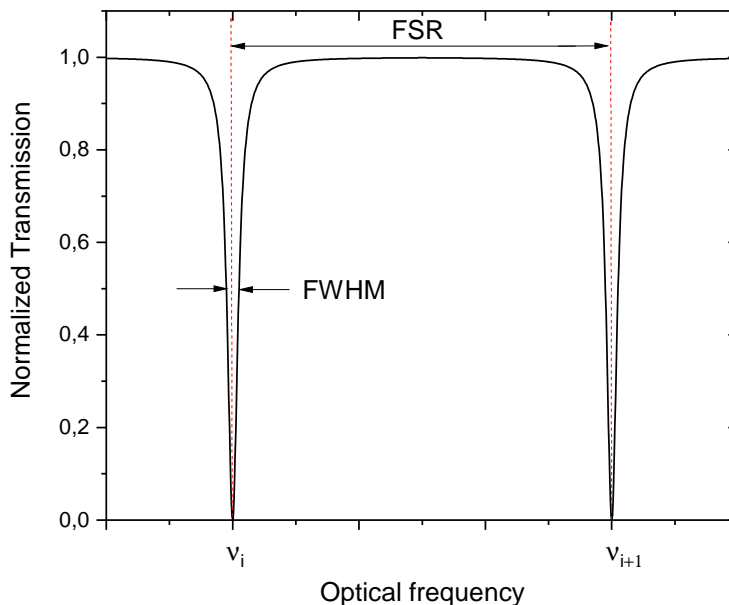


Figure 2: The calculated transmission spectrum of a general waveguide coupled with a WGM resonator. The transmitted power as a function of the optical frequency shows dips with Lorentzian shape. The individual dips occur at the frequencies of the modes of the resonator, with full width at half maximum (FWHM) linewidth  $\Delta\nu$  and the frequency spacing of free spectral range (FSR).

An essential parameter to evaluate the performance of a resonator is the quality factor (Q-factor) which is defined as the product of the given resonance frequency  $\nu_0$  and the photon lifetime  $\tau_0$  inside the resonator [23]:

$$Q = 2\pi\nu_0\tau_0 \quad (1.3)$$

A high Q-factor indicates a long photon lifetime. The Q-factor can alternatively be calculated as the ratio of the resonance frequency  $\nu_0$  and the full width at half maximum (FWHM) of the resonance linewidth  $\Delta\nu = 2\pi/\tau_0$  :

$$Q = \frac{\nu_0}{\Delta\nu} \quad (1.4)$$

With the spectrum in Figure 2 one obtains the loaded Q-factor (see Section 1.3). Both  $\nu_0$  and  $\Delta\nu$  can be measured from the transmission spectrum, providing an experimental method for the measurement of the Q-factor. In practice, as will be discussed in detail in Section 2.3, there exist some loss channels, for example, losses resulting from the leakage of light due to the curvature of the resonator, losses caused by absorption of the material itself and scattering due to the imperfection or roughness of the resonator surface, as well as in and out-coupling losses.

Other important parameters connected to the geometry of the resonators are the Finesse and the mode volume. The Finesse is defined as [24]:

$$\text{Finesse} = \frac{\Delta\nu_{\text{FSR}}}{\Delta\nu} \quad (1.5)$$

Which relates the free spectral range to the resonance linewidth and takes into consideration both the photon time and the resonator size [25].

The mode volume  $V_{\text{mode}}$  is defined as [26]:

$$V_{\text{mode}} = \frac{\int_V \varepsilon(\mathbf{r}) |\mathbf{E}(\mathbf{r})|^2 d^3\mathbf{r}}{\max[\varepsilon(\mathbf{r}) |\mathbf{E}(\mathbf{r})|^2]} \quad (1.6)$$

where  $\varepsilon(r)$  is the dielectric constant of the material,  $|E(r)|$  is the electric field, and  $V$  is the integration volume. A small mode volume leads to a significant enhancement of the nonlinear optical effects with low-power pumping to the resonators [27].

## 1.2 Total internal reflection and evanescent field

As anticipated, in WGM resonators, light is confined and propagates by continuous total internal reflection [28]. This phenomenon (see Figure 3) occurs for light waves traveling in a medium with refractive index  $n_1$  and incident into a medium with lower refractive index  $n_2$  with an incident angle  $\theta_i$  larger than the critical angle  $\theta_c = \arcsin(n_2/n_1)$ . Because of the cylindrical symmetry, in WGM resonators, all subsequent incident angles are the same as the initial incident angle, and therefore the ray of light is trapped.

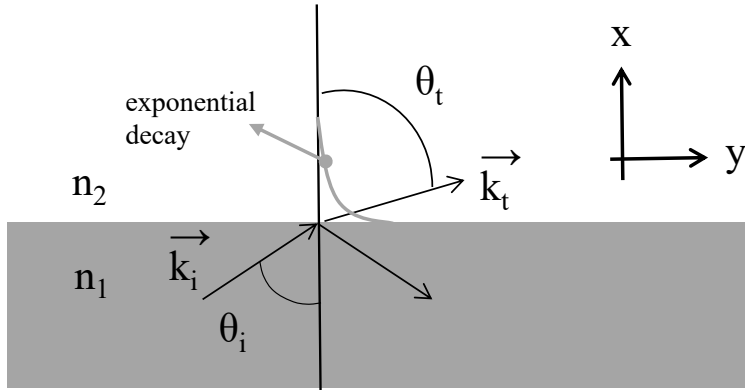


Figure 3: Reflection and refraction at an interface between two media with refractive indices  $n_1$  and  $n_2$ . The wave vectors of the incident wave and the refracted and transmitted waves are labeled as  $\vec{k}_i$  and  $\vec{k}_t$  respectively. For  $n_1 > n_2$  and incident angles larger than the critical angle  $\theta_c$ , the light field is totally reflected at the interface and there exists an electromagnetic field that decays exponentially beyond the interface. The penetration depth  $\delta$  of this evanescent field is typically on the order of the wavelength.

Additionally, under the total internal reflection condition, there still exists an electromagnetic field on the other side of the interface that decays exponentially in the lower refractive index medium. Therefore, the wave vector  $\vec{k}_t$  of the transmitted wave can be split into a component indicating the propagation along the interface and a component describing the propagation normal to the interface as [29]:

$$\vec{E}_t = E_{0t} \exp \left\{ i \vec{k}_t [(\cos \theta_t) \hat{x} + (\sin \theta_t) \hat{y}] \right\} \quad (1.7)$$

where,  $\theta_t$  is the angle of refraction and  $|\vec{k}_t| = n_2 2\pi/\lambda_0$ . According to Snell's

law:

$$n_1 \sin \theta_i = n_2 \sin \theta_t \quad (1.8)$$

the value for  $\cos \theta_t$  becomes imaginary when  $n_1 > n_2$  and  $\theta_i > \theta_c$ . So that

$$\cos \theta_t = \sqrt{1 - \sin^2 \theta_t} = i \sqrt{\left(\frac{n_1}{n_2}\right)^2 \sin^2 \theta_i - 1} \quad (1.9)$$

Since  $\cos \theta_t$  is purely imaginary, let's define a real quantity called  $\beta$  and it satisfies the equations  $k_t \cos \theta_t = i\beta$ . By substitution, the strength of the transmitted wave can thus be expressed as

$$E_t = E_{0t} \exp[-\beta x] \exp\left[ik_t \frac{n_1}{n_2} (\sin \theta_i) y\right] \quad (1.10)$$

The former exponential factor represents exponential damping in the x-direction, whereas the latter exponential factor denotes a traveling plane wave along the y-direction. This damped field is called the evanescent field. According to the damping factor in Equation (1.10), the strength of the decay wave could be described as [29]:

$$E(x) \sim e^{-x/\delta}$$

with

$$\delta = \frac{1}{\beta} = \left[ k_t \sqrt{\left(\frac{n_1}{n_2}\right)^2 \sin^2 \theta_i - 1} \right]^{-1} = \frac{\lambda_0}{2\pi \sqrt{n_1^2 \sin^2 \theta_i - n_2^2}} \quad (1.11)$$

which is typically on the order of wavelength  $\lambda_0$ . The strength of the evanescent field weakens exponentially as the distance away from the surface increases. The pronounced evanescent field can be used for light coupling between two optical components if they are close enough so that their evanescent fields overlap. In this experiment, light is coupled from an evanescent coupler to the resonator and vice versa. This phenomenon is known as “frustrated total internal reflection” where the evanescent field flows across the air and enters into a medium with a higher refractive index [30]. Thus the distance between the resonator and the evanescent coupler has to be on the order of the wavelength.

### 1.3 Light coupling methods

To measure the Q-factor in the frequency domain using Equation (1.4), the light has to be first coupled into the resonators. When a coupling element is present, energy is emitted from the resonator through this element. Therefore, the Q-factor which contains the energy loss due to the presence of the coupling element is referred to as the so-called “loaded Q-factor” through Equation (1.4). There are several methods to couple light into a WGM resonator by using evanescent couplers. This is achieved by overlapping the evanescent tails of the modes of the couplers with that of the WGMs. One of the techniques are prism couplers based on frustrated total internal reflection where the gap between the resonator and the prism can be optimized to accomplish critical coupling [31, 32]. But this method has some disadvantages. In particular, because the prism couplers are bulky, they are challenging to integrate with chip-based resonators.

In addition to prism couplers, angle-polished optical fibers [33] are also used for the excitation of WGMs. The resonator is positioned in the range of the evanescent field from the fiber core where an efficient energy exchange occurs between the waveguide mode and the WGMs.

Here, an alternative coupling method is chosen, which is the optical waveguide coupling using an optical nanofiber, realized as the waist of a tapered optical fiber as sketched in Figure 4, allowing for almost total power transfer to the WGMs. The nanofiber placed along the resonator enables easy alignment of the input mode, as well as collection of the output light [34]. It is possible to realize a coupling ideality (which is defined as the amount of power coupled into the desired mode) more than 99.97% [35] by using the optical nanofiber. In which the coupling strength can be modified by adjusting the distance between the nanofiber and the resonator. This means that the optical energy can be coupled both to and from the optical resonator with almost no loss [36].

A general description of the coupling of a resonator to an external light field is given in [37]. In Figure 4, the model is referred to the coupling junction between the nanofiber and the resonator by parameters  $\tau_0$  and  $\tau_e$ .  $\tau_0$  is associated with the energy decay rate of the mode due to internal dissipation in the resonator, whereas  $\tau_e$  describes the energy transfer between the external light field and the resonator mode. It is assumed that an external light field with angular frequency  $\omega$  and amplitude  $s$  propagating along the nanofiber

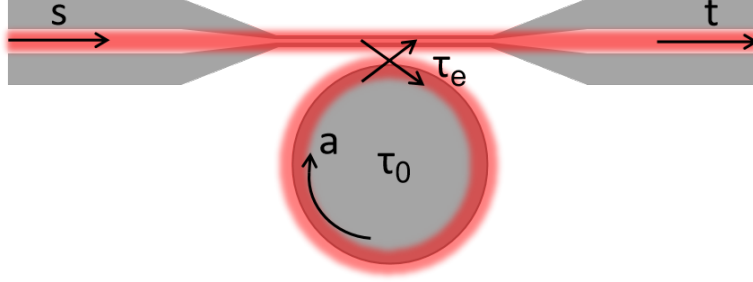


Figure 4: The model describing the coupling between the nanofiber and the WGM resonator. An input field with amplitude  $s$  is sent into the nanofiber. This input light field excites a resonator mode with amplitude  $a$ . The time constant  $\tau_0$  is associated with the energy decay rate of the mode due to internal dissipation in the resonator, whereas  $\tau_e$  describes the energy transfer between the external light field and the resonator mode. The coupling is monitored by the output field amplitude  $t$ .

excites a resonator mode with mode amplitude  $a$  and resonance frequency  $\omega_0$ . In this case, the temporal variation of  $a$  is given by

$$\frac{da}{dt} = i(\omega_0 - \omega) a - \frac{1}{2} \left( \frac{1}{\tau_0} + \frac{1}{\tau_e} \right) a + \sqrt{\frac{1}{\tau_e}} s \quad (1.12)$$

The first term implies that the resonance condition must be fulfilled in order for power to build up in the resonator. The second term describes the decay of the mode amplitude due to intrinsic resonator losses  $\tau_0$  and the losses caused by the nanofiber  $\tau_e$ . The third term represents the coupling to the external driving light field.

Hence, in the absence of an external driving light field, the decay rate of the energy  $W$  is:

$$\frac{dW}{dt} = a^* \frac{da}{dt} + a \frac{da^*}{dt} = - \left( \frac{1}{\tau_0} + \frac{1}{\tau_e} \right) W \quad (1.13)$$

where  $W = |a|^2 = aa^*$ . In this case, the energy stored in the resonator decays due to the resonator's intrinsic losses and the energy coupled back to the nanofiber. The transfer of optical energy between the guided mode of the nanofiber and the resonator mode strongly relies on the spatial overlap between the evanescent fields of both components. As a result, varying the distance of the coupling gap yields a different value for  $\tau_e$ . Equation (1.13) gives the following solution:

$$W = W_0 \exp \left( -t (\tau_0^{-1} + \tau_e^{-1}) \right) = W_0 \exp \left( -t / \tau_{\text{load}} \right) \quad (1.14)$$

where  $\tau_{\text{load}}^{-1} = \tau_0^{-1} + \tau_e^{-1}$  is the overall decay rate of the energy in such a nanofiber-resonator system. As a consequence, the Q-factor in the presence of the nanofiber turns out to be  $Q_{\text{load}} = 2\pi\nu_0\tau_{\text{load}} = \omega_0\tau_{\text{load}}$ , and it can be written in separated terms:

$$Q_{\text{load}}^{-1} = (\omega\tau_0)^{-1} + (\omega\tau_e)^{-1} = Q_0^{-1} + Q_e^{-1} \quad (1.15)$$

where the intrinsic Q-factor  $Q_0$  only contains the intrinsic resonator losses.

At a steady state, the rate of energy lost from the resonator equals the rate of energy entering the resonator. If the external driving field is at frequency  $\omega$ , the solution of Equation (1.12) is:

$$a = \frac{s\tau_e^{-1/2}}{i(\omega - \omega_0) + 1/2(\tau_0^{-1} + \tau_e^{-1})} \quad (1.16)$$

To estimate the nanofiber transmission  $T = |t/s|^2$  for an arbitrary excitation, it is useful to develop an equation for the output field amplitude  $t$ . For a linear system,  $t$  is proportional to the sum of the input field amplitude  $s$  and the resonator mode amplitude  $a$  weighted with appropriate coefficients  $c_s$  and  $c_a$ , respectively:

$$t = c_s s + c_a a \quad (1.17)$$

According to Equation (1.12), in the absence of external driving field ( $s = 0$ ) and without the intrinsic losses  $\tau_0 = 0$ , the mode decays at the rate  $1/\tau_e$  because the transmitted waves take away the power. From Equation (1.12) with ( $s = 0$ ) and energy conservation:

$$\frac{d}{dt}|a|^2 = -\frac{1}{\tau_e}|a|^2 = -|t|^2 \quad (1.18)$$

Thus,

$$t = \sqrt{\frac{1}{\tau_e}}a = c_a a \quad (1.19)$$

and

$$c_a = -\sqrt{\frac{1}{\tau_e}} \quad (1.20)$$

The second coefficient  $c_s$  can again be evaluated using energy conservation, which implies that the power incident to the resonator equals the build-up energy in the resonator plus the energy dissipation from intrinsic losses:

$$|s|^2 - |t|^2 = \frac{d}{dt}|a|^2 + \frac{1}{\tau_0}|a|^2 \quad (1.21)$$

From Equation (1.12), one has:

$$\frac{d}{dt}|a|^2 = -\left(\frac{1}{\tau_0} + \frac{1}{\tau_e}\right)|a|^2 + \sqrt{\frac{1}{\tau_e}}(a^*s + as^*) \quad (1.22)$$

Substituting Equation (1.22) to (1.21) gives:

$$-\frac{1}{\tau_e}|a|^2 + \sqrt{\frac{1}{\tau_e}}(a^*s + as^*) = |s|^2 - |t|^2 \quad (1.23)$$

Eliminating coefficient  $c_s$  from Equation (1.23) by combining Equation (1.17) together with Equation (1.20) gives the coefficient  $c_s = 1$ .

Therefore, Equation (1.17) representing the output field amplitude of the nanofiber has the form:

$$t = -s + \sqrt{\frac{1}{\tau_e}}a \quad (1.24)$$

Inserting Equation (1.16) leads to:

$$\frac{t}{s} = \frac{1/2(\tau_e^{-1} - \tau_0^{-1}) + i(\omega - \omega_0)}{1/2(\tau_e^{-1} + \tau_0^{-1}) + i(\omega - \omega_0)} \quad (1.25)$$

The transmission  $T = |t/s|^2$  is a function of the frequency  $\nu = \omega/2\pi$  which has a Lorentzian shape centered around the resonance frequency  $\nu_0$ . And  $\Delta\omega = 2\pi\Delta\nu = \tau_e^{-1} + \tau_0^{-1} = \tau_{\text{load}}^{-1}$  is the FWHM of a Lorentzian, which is related to the loaded Q-factor by Equation (1.4) and (1.15). Here,  $\tau_e$  depends on the nanofiber-resonator distance, and decreasing the distance leads to a decrease in the loaded Q-factor, which can be observed in a broader FWHM in the nanofiber power transmission spectrum.

From Equation (1.25), one can derive the on-resonance transmission  $T_{\text{res}} = T(\omega = \omega_0)$ :

$$T_{\text{res}} = \left(\frac{\tau_e^{-1} - \tau_0^{-1}}{\tau_e^{-1} + \tau_0^{-1}}\right)^2 \quad (1.26)$$

According to [38], different coupling regimes can be determined by the ratio of  $\tau_0/\tau_e$ .

**1. Under-coupled regime**  $\tau_0/\tau_e < 1$ . When the nanofiber-resonator distance is large and  $\tau_e \gg \tau_0$ , only a small portion of the power transmitted

through the nanofiber enters the resonator. Thus  $T_{\text{res}}$  is close to unity, and it drops as the nanofiber-resonator distance decreases since there is more power coupling from the nanofiber to the resonator. This regime is called under-coupled because the incoupling rate to the resonator is smaller than the resonator's intrinsic loss rate and the nanofiber transmission is always above zero.

**2. Critically-coupled regime**  $\tau_0/\tau_e = 1$ . For a certain nanofiber-resonator distance, the incoupling rate  $1/\tau_e$  equals the resonator intrinsic loss rate  $1/\tau_0$  associated with  $\tau_0$ , meaning that the power transmitted through the nanofiber is totally dissipated in the resonator. This regime is denoted as critically-coupled. According to Equation (1.15), the loaded Q-factor in the critically-coupled regime  $Q_{\text{crit}}$  is:

$$Q_{\text{crit}} = \frac{\omega_0 \tau_0}{2} = \frac{Q_0}{2} \quad (1.27)$$

thus the measured  $Q_{\text{crit}}$  is half of the intrinsic Q-factor and thus the intrinsic Q-factor can be easily calculated in the critically-coupled regime. In this thesis, the  $Q_{\text{crit}}$  is measured in the frequency domain, according to Equation (1.4), one has

$$Q_{\text{crit}} = \frac{\nu_0}{\Delta\nu_{\text{measured}}} = \frac{Q_0}{2} \quad (1.28)$$

with  $2\pi\Delta\nu_{\text{measured}} = \tau_e^{-1} + \tau_0^{-1} = 2\tau_0^{-1}$ .

**3. Over-coupled regime**  $\tau_0/\tau_e > 1$ . When further decreasing the nanofiber-resonator distance, the amplitude of the resonator field coupling back to the nanofiber exceeds the field of the nanofiber, resulting in a recovery in the transmission  $T_{\text{res}}$ . This regime is known as over-coupled.

The transmission spectra illustrating the under-coupled, critically-coupled, and over-coupled regimes are shown in Figure 5. From the under-coupled to the critically-coupled regime, the transmission drops as the FWHM increases, and it achieves its minimal value in the critically-coupled regime. From critically-coupled to over-coupled regime, the transmission recovers as the FWHM increases even further.

Alternatively, the on-resonance transmission can be described in terms of the coupling parameter  $K$ :

$$T = \left( \frac{1 - K}{1 + K} \right)^2 \quad (1.29)$$

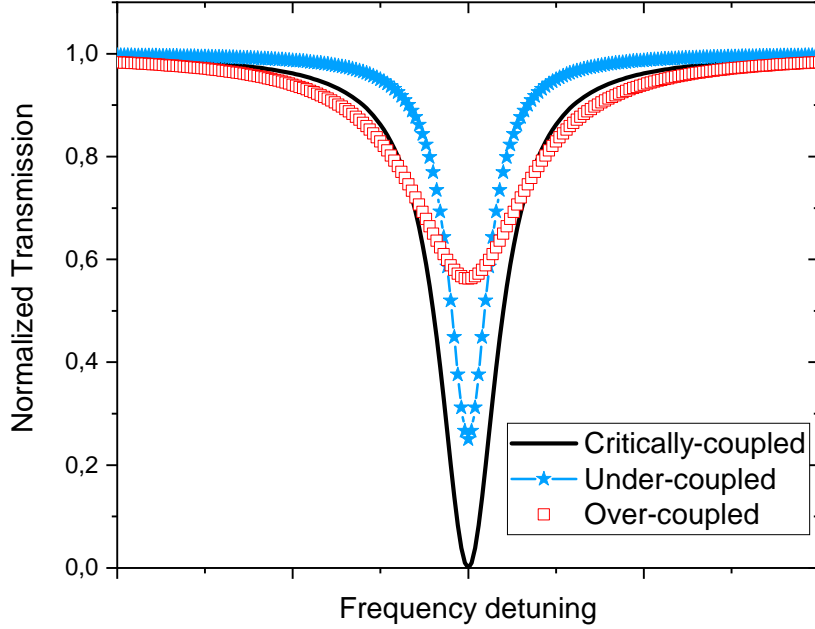


Figure 5: Calculated power transmission spectra illustrating the under-coupled, critically-coupled, and over-coupled regimes.

the  $K$  is defined as the ratio of the coupling between the fundamental mode of nanofiber and the resonator mode  $\kappa_e$ , to the coupling of all other loss channels:

$$K = \frac{\kappa_e}{\kappa_{para} + \kappa_0} \quad (1.30)$$

with  $\kappa_e = \tau_e^{-1}$ .  $\kappa_0 = \tau_0^{-1}$  is the rate of coupling to the intrinsic loss channels and  $\kappa_{para} = \tau_{para}^{-1}$  is the rate of coupling to the parasitic loss channels, which for example, could come from the scattering at the coupling junction of nanofiber-resonator.

With this formalism, the three coupling regimes can be classified using this coupling parameter  $K$ .  $K = 1$  stands for critically-coupled while  $K < 1$  and  $K > 1$  represent under-coupled and over-coupled respectively.

## 2 Silica on silicon microdisk resonators

### 2.1 Fabrication and morphological characterization of on-chip microdisk resonator

The silica-on-silicon microdisk resonators studied in this thesis are fabricated at the Ferdinand-Braun-Institut according to the procedure [39] summarized in the following.

The starting point consists of a silicon chip with a thermally-grown silicon oxide layer. The thickness of this oxide layer can vary from a few hundred nanometers to a few microns and determines the thickness of the final microdisk.

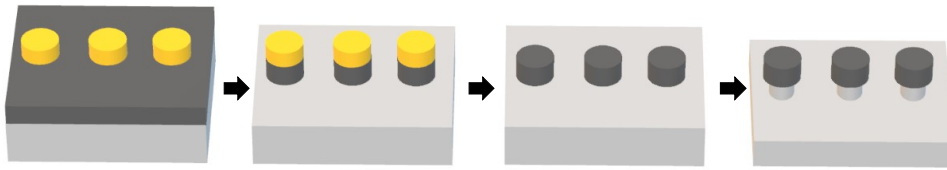


Figure 6: Fabrication steps of on-chip microdisk resonators used in this thesis which are made of silica (dark grey) on silicon (light grey).

At first, the silica-on-silicon chip is coated with a photoresist and patterned by a stepper lithography process creating the lateral geometry of the disk layout. The photoresist is then exposed, and developed, leaving on the silica layer the desired pattern (yellow disks in Figure 6). The silica without photoresist on top (dark grey in Figure 6) is removed according to the pattern using reactive ion etching (RIE) and plasma etching to form the oxide pillars, typically based on carbon tetrafluoride ( $\text{CF}_4$ ). If wedges are desired, the resist pattern can undergo a so-called “reflow”. The wafer is placed on a hot plate at  $180^\circ\text{C}$  for 3 minutes during the reflow to soften the photoresist and allow it to reflow to a more spherical shape creating a contact angle of about  $15^\circ$ . The wedge angle is then transferred into the oxide layer by etching according to the selectivity of the etch recipe. After a cleaning process to remove the photoresist, the silicon (light grey in Figure 6) is isotropically undercut by wet chemistry etching to form the WGM resonator.

With this fabrication protocol, silica microdisks with a diameter between  $50\ \mu\text{m}$  to  $480\ \mu\text{m}$ , thickness between  $380\ \text{nm}$  to  $4\ \mu\text{m}$ , and undercut with a distance from the resonator to the substrate between  $100\ \text{nm}$  to  $6.5\ \mu\text{m}$  can be fabricated.

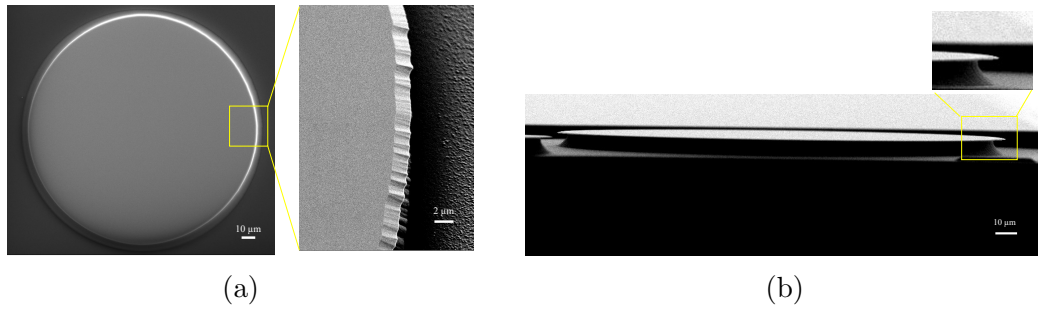


Figure 7: (a) Top view SEM micrograph of a disk resonator after fabrication. The zoom-in image shows the roughness of the edge is around  $300\ \text{nm}$ . (b) SEM micrograph of the same disk resonator taken from a tilted view: the distance from the resonator disk to the substrate is about  $6.5\ \mu\text{m}$ .

Typical scanning electron microscopy (SEM) images of a  $200\ \mu\text{m}$  diameter disk resonator are presented in Figure 7 at different angles and magnification.

The top view of the microdisk in Figure 7(a) shows a smooth and clean surface. At a closer look, the disk rim can present a roughness of around  $300\ \text{nm}$  indicating that the etching step was not optimal. Figure 7(b) is a side view of the same structure and allows to estimate of the distance between the suspended silica resonator and the silicon substrate, which is about  $6.5\ \mu\text{m}$  in this case.

As will be discussed in detail in Chapter 3, for our experiment, the layout of the microdisks on the chip is designed to have the resonators as close to the chip corner as possible. This design imposes careful handling of the samples that can easily get contaminated.

Figure 8(a) is an optical microscope image of a chip contaminated due to improper handling when taking it out of the sample box, where the green circular section of the microdisk is the suspended part of the silica. As a possible cleaning process, the first try is washing the sample with acetone and gently drying it with nitrogen, but one could not observe any macroscopic improvement. We then softly wiped the chip with a lens cleaning paper wetted with acetone. Figure 8(b) and (c) show that one but best two wipes are sufficient to remove most of the contaminants.

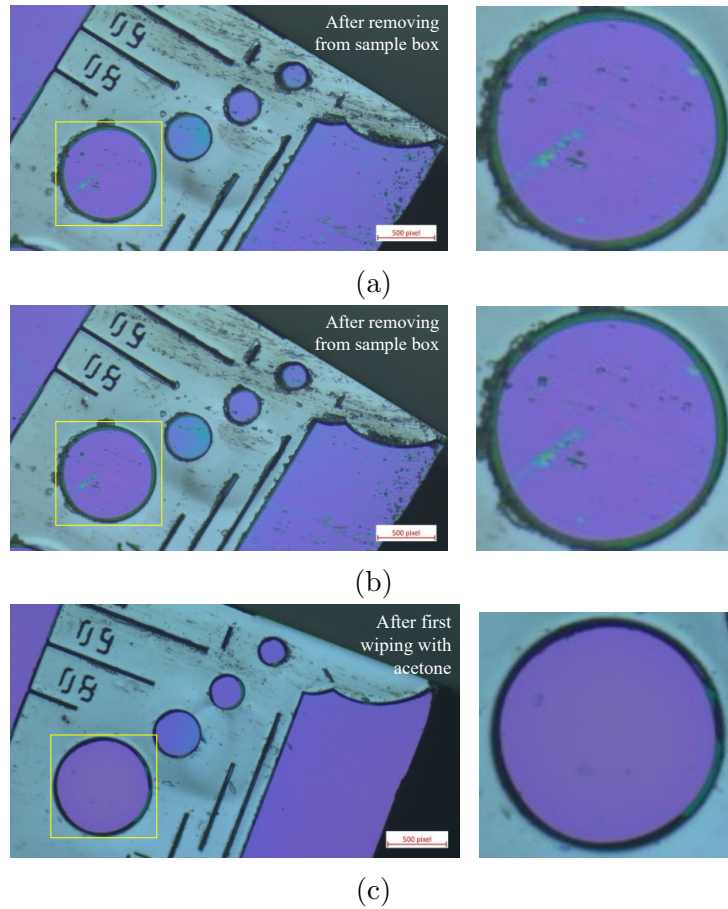


Figure 8: (a) Microscope image of a chip that is contaminated due to improper handling. The green circular section of the microdisk is the suspended part of the silica. (b) Most contaminants are removed by wiping the sample with optical paper wetted with acetone. (c) Image of the chip after the second cleaning by wiping with acetone, almost all contaminants are removed.

This process is however too aggressive for the sample. As shown in Figure 9(a) and (b), compared with Figure 8, the suspended part of the disk is completely destroyed by the cleaning process. For our study, we therefore selected samples fabricated with the optimized lithographic process and pay particular attention to handling the sample with tweezers, to avoid contamination.

The morphology of the disk resonator, which is the one in the yellow frame as shown in Figure 8, after the second cleaning is shown in SEM micrographs in Figure 9. The chipped edge of the resonator shown in Figure 9(a) from the

top view indicates that the extended part of the silica is destroyed due to the cleaning process mentioned above. This can also be seen from Figure 9(b) where the extended rim of the microdisk is no longer present.

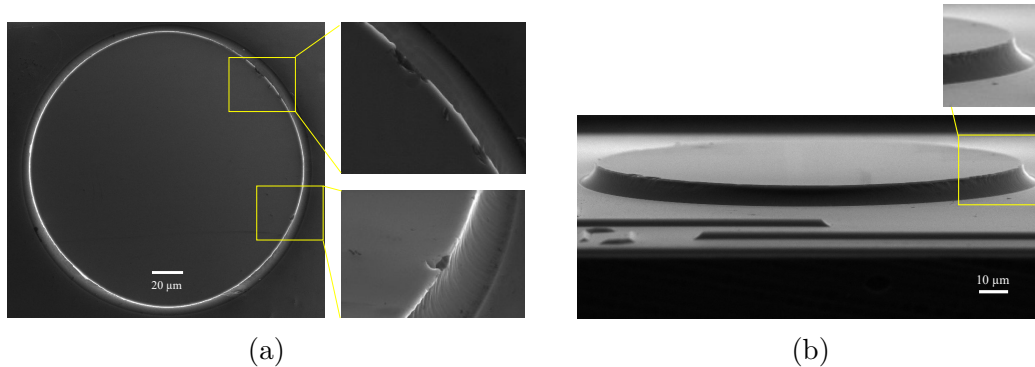


Figure 9: (a) Top view SEM micrograph of a disk resonator (the one in the yellow frame as shown in Figure 8 after the second cleaning). The zoom-in image shows that the edge is chipped. (b) SEM micrograph of the same disk resonator taken from a tilted view showing that the extended rim of the silica is completely destroyed.

From the study of morphology, one learns that the fabrication process has a significant influence on the quality of the microdisk. Moreover, one should be careful when dealing with the sample chips because of the customized layout of microdisks, which places the disks close to the edges of the chip's corner.

## 2.2 Mode analysis of microdisk resonators

The ray optics description of WGMs provided in Chapter 1 has limitations since it cannot account for the polarization of light. While in the wave optics domain, the electromagnetic theory can offer a complete description of the WGMs. WGM resonators support modes of two perpendicular polarizations, which are transverse electric (TE) modes and transverse magnetic (TM) modes. Since the microdisk resonator has cylindrical symmetry, the optical modes can be calculated by solving the Helmholtz equation in cylindrical coordinates as discussed in detail in this section. In TM modes,  $E_z = 0$ , only the components  $H_z$ ,  $E_r$  and  $E_\varphi$  contribute to the electromagnetic field. In TE modes,  $H_z = 0$ , only the components  $E_z$ ,  $H_r$  and  $H_\varphi$  contribute to the electromagnetic field. Thus, it is useful to solve for the  $z$ -components of

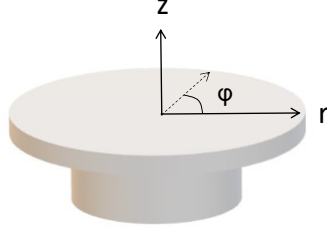


Figure 10: Schematic of the microdisk resonator. The Helmholtz equation (Equation 2.1) is solved in cylindrical coordinates with radial coordinate and the axial coordinate denoted by  $r$  and  $z$  respectively, and  $\varphi$  the azimuthal coordinate.

electromagnetic field propagating in such structures and then use Maxwell's equations to derive the other components.

The  $z$ -components of the electromagnetic field for a microdisk resonator is described by the Helmholtz equation:

$$\begin{aligned} \left(\nabla^2 + k^2 n^2\right) \cdot \vec{E}_z &= 0 \\ \left(\nabla^2 + k^2 n^2\right) \cdot \vec{H}_z &= 0 \end{aligned} \quad (2.1)$$

where  $\nabla^2$  is the Laplace operator and  $n$  is the refractive index of the medium. Here,  $k = 2\pi/\lambda_0 = \omega/c$  is the vacuum wavenumber with vacuum wavelength  $\lambda_0$  and angular frequency  $\omega$ .  $c$  is the vacuum speed of light. In cylindrical coordinates, as shown in Figure 10, the Laplace operator reads:

$$\vec{\nabla}^2 = \frac{1}{r} \partial_r + \partial_r^2 + \frac{1}{r^2} \partial_\phi^2 + \partial_z^2 \quad (2.2)$$

where  $z$  and  $r$  are axial coordinate and radial coordinate, respectively, and  $\varphi$  is azimuthal coordinate. For a microresonator with a thickness of only a fraction of the mode wavelength, the analysis of the modes can be studied in the 2D approximation in which the coordinate dependence of the electromagnetic field in the  $z$  direction can be omitted using the effective refractive index  $n(x, y) = n(r, \varphi)$  [40].

According to Equation (2.1), for TE-modes ( $H_z = 0$ ) one has:

$$\frac{\partial^2 E_z}{\partial r^2} + \frac{1}{r} \frac{\partial E_z}{\partial r} + \frac{1}{r^2} \frac{\partial^2 E_z}{\partial \varphi^2} + k^2 n^2(r, \varphi) E_z = 0 \quad (2.3)$$

with

$$H_r = \frac{i}{\mu\omega} \frac{\partial E_z}{\partial \varphi}, \quad H_\varphi = -\frac{i}{\mu\omega} \frac{\partial E_z}{\partial r} \quad (2.4)$$

where  $\mu$  is the permeability of the medium and  $\vec{\nabla} \times \vec{E} = -\mu \frac{\partial \vec{H}}{\partial t} = -\mu i\omega \vec{H}$ . Here,  $\nabla$  is the nabla operator.

For TM-modes ( $E_z = 0$ ) one has:

$$\frac{\partial^2 H_z}{\partial r^2} + \frac{1}{r} \frac{\partial H_z}{\partial r} + \frac{1}{r^2} \frac{\partial^2 H_z}{\partial \varphi^2} + k^2 n^2(r, \varphi) H_z = 0 \quad (2.5)$$

with

$$E_r = \frac{-i}{\epsilon\omega} \frac{1}{r} \frac{\partial H_z}{\partial \varphi}, \quad E_\varphi = \frac{i}{\epsilon\omega} \frac{\partial H_z}{\partial r} \quad (2.6)$$

where  $\epsilon$  is the permittivity of the medium and  $\vec{\nabla} \times \vec{H} = \epsilon \frac{\partial \vec{E}}{\partial t} = \epsilon i\omega \vec{E}$ .

For a homogeneous microdisk of radius  $R$  the effective refractive index  $n(r, \varphi) \equiv n$  if  $r < R$ . Thus, inside the microdisk, Equation (2.3) and (2.5) can be written as:

$$\frac{\partial^2 \psi}{\partial r^2} + \frac{1}{r} \frac{\partial \psi}{\partial r} + \frac{1}{r^2} \frac{\partial^2 \psi}{\partial \varphi^2} + k^2 n^2 \psi = 0 \quad (2.7)$$

where  $\psi = E_z$  or  $\psi = H_z$ .

Separation of variables gives the solution that the field function has the form [40]:

$$\psi = \begin{cases} A_m J_m(knr) e^{im\varphi} & r < R \text{ (inside the resonator)} \\ B_m Y_m(kr) e^{im\varphi} & r \geq R \text{ (outside the resonator)} \end{cases} \quad (2.8)$$

where  $J_m$  and  $H_m$  are Bessel functions of the first and second kind respectively. The azimuthal component of the wave function is given by  $e^{im\varphi}$  because of the cylindrical symmetry, while  $m$  is the azimuthal modal index.

In Equation (2.8), the refractive index of the environment is air and it is fixed to be 1 if  $r > R$ . Then, the boundary conditions at the interface  $r = R$  lead to a set of independent transcendental equations for the microdisk resonances with wave number  $k_{res}$  [40, 41]:

$$\begin{aligned} n \frac{J'_m(k_{res}nR)}{J_m(k_0nR)} - \frac{Y'_m(k_{res}nR)}{Y_m(k_{res}nR)} &= 0 \quad (TM) \\ \frac{J'_m(k_{res}nR)}{J_m(k_{res}nR)} - n \frac{Y'_m(k_{res}nR)}{Y_m(k_{res}nR)} &= 0 \quad (TE) \end{aligned} \quad (2.9)$$

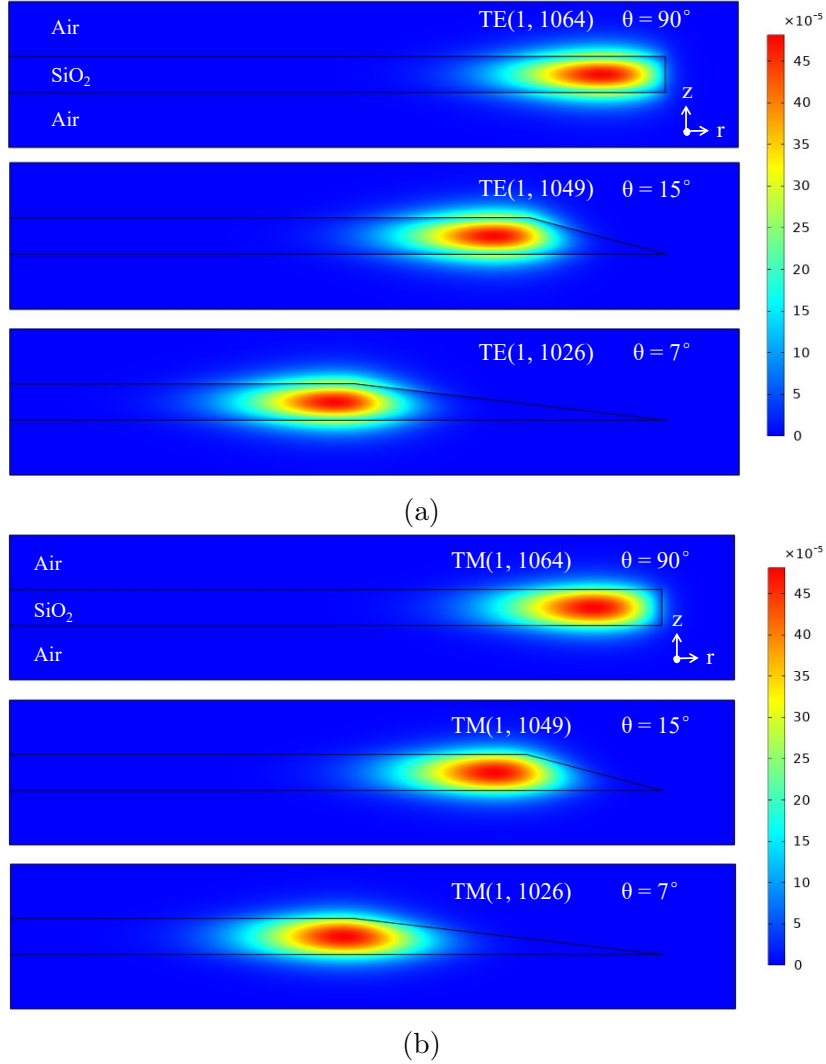


Figure 11: Fundamental mode intensity profiles in  $r - z$  plane (as sketched in Figure 10) of the  $200\ \mu\text{m}$ -diameter large,  $500\ \text{nm}$ -thick silica microdisk resonators (black solid lines) with  $90^\circ$ ,  $15^\circ$ ,  $7^\circ$  (the measured microdisks in this thesis) wedge angles. The first and second values in parenthesis stand for the radial mode number and the azimuthal mode number respectively. (a) TE mode intensity profiles. Along the  $z$  axis, the evanescent field is more pronounced. (b) TM mode intensity profiles. The evanescent field is pronounced along the  $r$  direction.

Figure 11 is a simulation of the fundamental TE and TM mode intensity profiles in the  $200\ \mu\text{m}$ -diameter large,  $500\ \text{nm}$ -thick silica microdisk resonators with  $90^\circ$ ,  $15^\circ$ ,  $7^\circ$  wedge angles. The mode is found at the wavelength of

around 785 nm, which falls in the wavelength tuning range of the distributed feedback (DFB) diode laser used in this thesis to excite the resonator modes, as will be introduced in the next chapter. The evanescent field outside the resonator decays at a length scale of a few hundred nanometers. For TE mode the evanescent field is more pronounced in the vertical direction whereas for TM mode evanescent field pronounce laterally. Additionally, Figure 11 is shown as an example of how the wedge affects the fundamental mode distribution at different wedge angles and for smaller wedge angles the modes are inner. As a result, the fundamental modes of the wedge resonator are pushed far away from the scattering edge of the device and, hence, suffer less from surface-induced losses [42]. In this thesis, the measured microdisks are with a wedge angle of 7°.

### 2.3 Preliminary consideration of Q-factor

In order to have a pre-analysis of the intrinsic Q-factor  $Q_0$ , it is essential to investigate the source of losses which affect  $Q_0$ . The intrinsic Q-factor of a WGM resonator is linked by many mechanisms. The material loss of the resonator ( $Q_{\text{mat}}$ ), the scattering from imperfections of resonator surface ( $Q_{\text{surface}}$ ), and the light leakage during total internal reflections at a curved surface ( $Q_{\text{rad}}$ ) all contribute to the intrinsic losses by [43]:

$$Q_0^{-1} = Q_{\text{mat}}^{-1} + Q_{\text{surface}}^{-1} + Q_{\text{rad}}^{-1} \quad (2.10)$$

The material-related losses in microresonators come from the absorption of the material and Rayleigh scattering. Using the absorption coefficient  $\alpha$  which includes both absorption and Rayleigh scattering effects, describing the power attenuation per unit length, the material-related Q-factor ( $Q_{\text{mat}}$ ) is evaluated using the equation [44]:

$$Q_{\text{mat}} = \frac{2\pi n}{\alpha\lambda} \quad (2.11)$$

where  $n$ , and  $\lambda$  are the refractive index of the material and the resonance wavelength of the resonator, respectively.

For microdisk resonators with a thickness of a fraction of the wavelength, contamination by dust particles on the surface and surface roughness have a considerable influence on the intrinsic Q-factor, referring to surface-related losses. As will be mentioned in Chapter 3, both the nanofiber and the microdisks are kept in a home-built flow box to minimize dust contamination.

And the fabrication process for the silica microdisk described in Section 2.1 is capable of producing disks with very smooth top and bottom surfaces to maintain high Q-factor. The Q-factor related to surface roughness  $Q_{ss}$  is given as [43]:

$$Q_{ss} \approx \frac{3\lambda^3 R}{8\pi^2 \bar{n} B^2 s^2} \quad (2.12)$$

where  $s$  is the root mean square size (r.m.s) of the surface roughness, and  $B$  is the correlation length of the roughness. By testing it at various wavelengths, it is possible to determine if the Q-factor is mainly limited by the surface roughness because of the  $\lambda^3$  dependence. The atomic force microscope (AFM) measurement of the top surface of the fabricated microdisk results in 0.3 nm r.m.s [39].

The last term  $Q_{rad}$  in Equation (2.10) related to radiation losses is given by [43]:

$$Q_{rad} \approx \frac{2\pi R}{\lambda} \frac{\zeta e^{2T}}{\sqrt{\bar{n}^2 - 1}} \quad (2.13)$$

with

$$T = \frac{2\pi R}{\lambda} \left( \cosh^{-1} \bar{n} - \sqrt{\bar{n} - \bar{n}^{-1}} \right) \quad (2.14)$$

where the relative refractive index is given by  $\bar{n} = n/n_0$ , the ratio of the refractive index of the resonator and its surroundings. For TE mode  $\zeta = 1$  and for TM mode  $\zeta = n^{-2}$ .  $R$  and  $\lambda$  are the radius and resonance wavelength of the resonator respectively. For a 200  $\mu\text{m}$  diameter silica microdisk, one has  $T \sim 10^3$ , leading to an enormous  $Q_{rad}$  which is negligible in the overall contribution to intrinsic Q-factor  $Q_0$  according to Equation (2.10).

As a result, the intrinsic Q-factor for a resonator in this thesis is dominated by absorption and surface-related losses.

### 3 Experimental method for Q-factor measurement

#### 3.1 Optomechanical setup

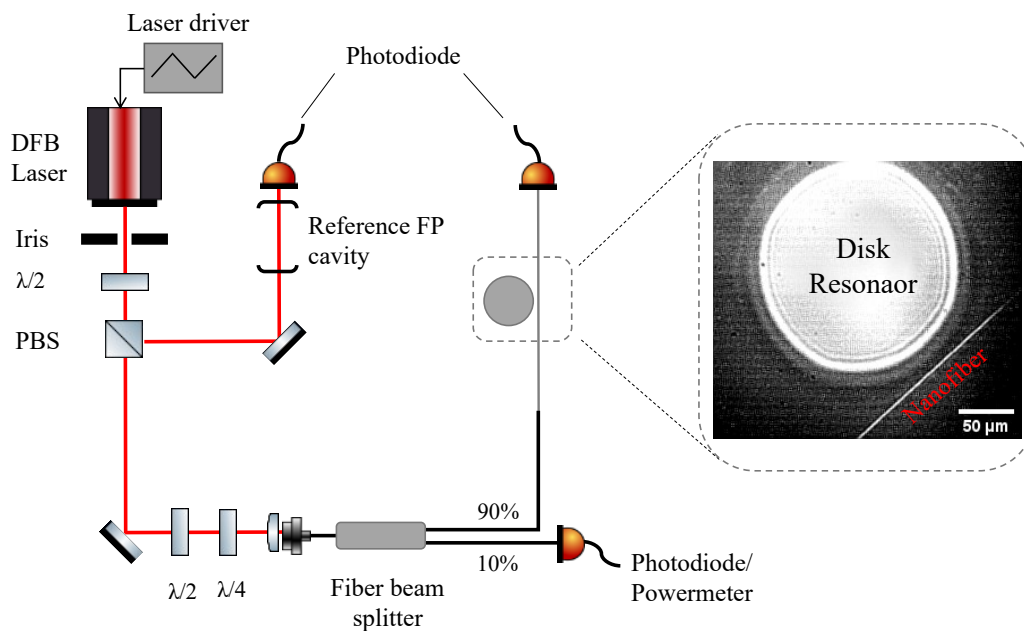


Figure 12: Schematic of the experimental setup implemented during this thesis for the characterization of optical disk resonators on the chip.

The experimental setup built during this thesis to measure the Q-factor of the microdisk resonators introduced in Chapter 2 is sketched in Figure 12 and its key components are discussed hereafter. Basically, a tunable laser is sent into an optical nanofiber (described in detail in Section 3.2) and its transmission is monitored in real-time while changing the nanofiber-resonator distance.

Light coupling to the resonator is done by using an optical nanofiber, which relies on the overlap of the evanescent fields of the two components as specified in Chapter 1. Therefore, submicrometer-level control of the nanofiber-resonator distance is required. Furthermore, because both the resonators and the nanofiber are sensitive to dust and other contaminants, they are hosted in a home-built flow box.

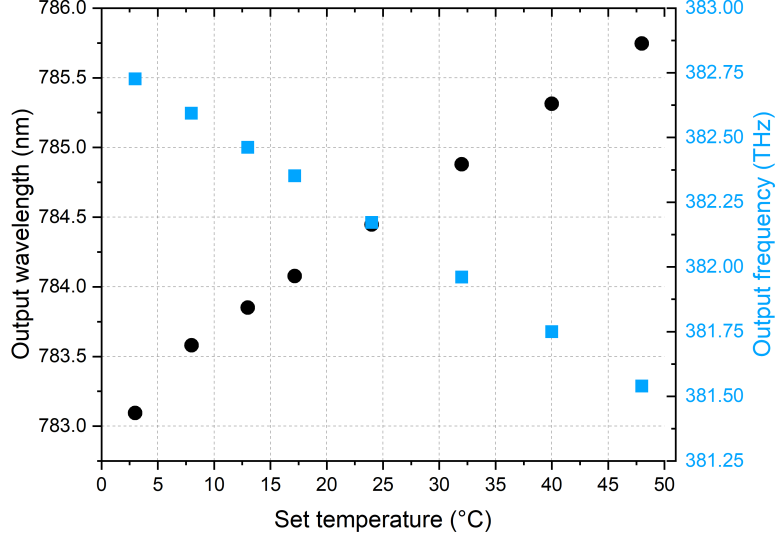


Figure 13: Laser output wavelength and frequency for different laser temperatures.

**DFB diode laser at a wavelength of 785 nm** The tunable laser used in this thesis to explore the spectral features of the resonator is a distributed feedback (DFB) diode laser (Toptica Photonics, DLC Pro). It has a 2.4 nm mode-hop-free wavelength tuning range around the center wavelength of 784.2 nm and a linewidth  $\Delta\nu_{\text{probe}} = 500$  kHz. In order to obtain the FWHM linewidth  $\Delta\nu$ , the laser frequency is scanned over the resonance frequency of the resonator mode. Thus the linewidth of the probe laser  $\Delta\nu_{\text{probe}}$  has a contribution to the measured linewidth. Consequently, the condition  $\Delta\nu_{\text{probe}} \ll \Delta\nu$  has to be fulfilled.

The output frequency of this DFB diode laser can be tuned by changing the diode's current or temperature. For current control, the total frequency scanning range is about 16 GHz while for temperature control, the total scanning range is about 1 THz. An arbitrary waveform generator is used to scan the laser frequency by temperature modulation.

A characterization curve of the DFB diode laser output wavelength and frequency for different temperatures is plotted in Figure 13. The laser output is measured with a wavemeter (Coherent, WaveMaster) for a fixed current of 60 mA.

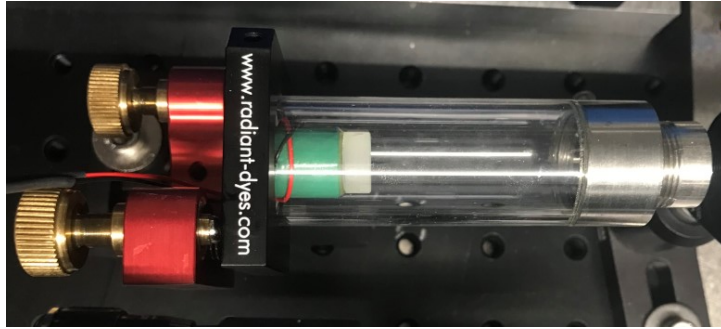


Figure 14: Picture of the confocal Fabry-Pérot cavity used as a reference cavity for the frequency tuning of the laser.

**Fabry-Pérot reference cavity** To monitor in real-time the laser frequency tuning and to perform the time-to-frequency conversion, a portion of the laser light is sent into a home-built Fabry-Pérot cavity (1.5 GHz free spectral range).

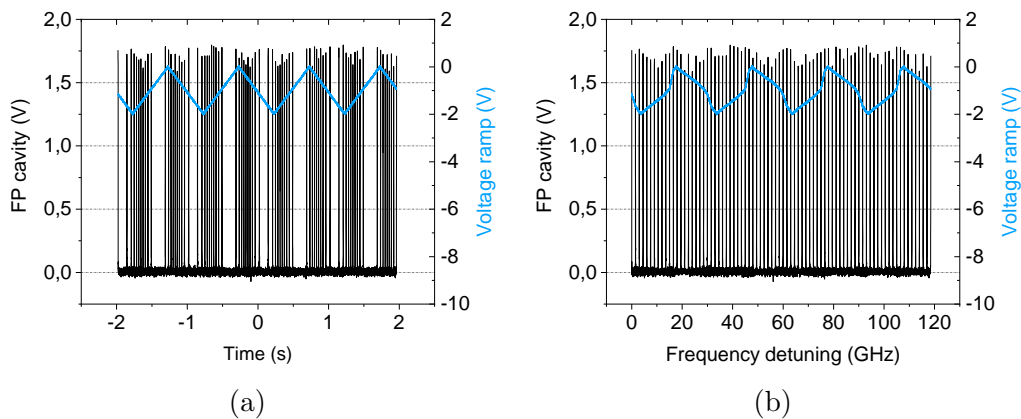


Figure 15: (a) Transmission profile of a confocal Fabry-Pérot cavity when applying linear and symmetric scanning voltage ramp in time. The resonance peaks are not equally spaced in time. (b) Transmission profile in frequency after time-to-frequency conversion, with the frequency spacing of each peak to be 1.5 GHz.

Figure 15(a) plots a typical transmission profile of the Fabry-Pérot cavity (black line) together with the linear and symmetric voltage ramp (blue line) sent to the laser temperature controller. Let us notice that the relative distance between subsequent peaks known to be equal to the FSR of 1.5 GHz,

is not even. This is due to a non-perfectly linear response of the laser to the applied ramp, especially at the ramp's turning points. Figure 15(b) shows the transmission profile in frequency after applying the time-to-frequency conversion.

**Other components** A combination of half and quarter wave plates allows to enhance coupling efficiency between the nanofiber and the resonator by control of the polarization.

A 90/10 fiber beam splitter is used to measure the power sent into the nanofiber by connecting the 10% output port to a photodiode (Thorlabs, DET36A) and the 90% output port to the nanofiber's input. A second photodiode (Thorlabs, PDA36A2) is used to measure the transmitted power of the nanofiber. All the photodiode signals are captured by a digital oscilloscope (Keysight, MSOS804A) with a sample rate of 10 GSa/s and analog bandwidth of 8 GHz.



Figure 16: Schematic of the customized nanofiber holder where the two tapered ends are attached with UV curing glue.

**Nanofiber holder** The nanofiber is mounted on a customized holder (sketched in Figure 16), with both tapered ends attached with UV curing glue to maintain the fiber's stability.

**Position control of the nanofiber** The positioning system is shown in Figure 17(a) and comprises three orthogonally stacked translation stages for coarse placement. They are driven by stepper motors (Physik Instrumente, M-232) with a displacement range of 17 mm and the smallest step size of 1  $\mu\text{m}$ . Two extra piezoelectric micron screws (Physik Instrumente, P-854)

allow for fine adjustment over a distance of  $25\ \mu\text{m}$  with a step size of less than  $1\ \text{nm}$ .

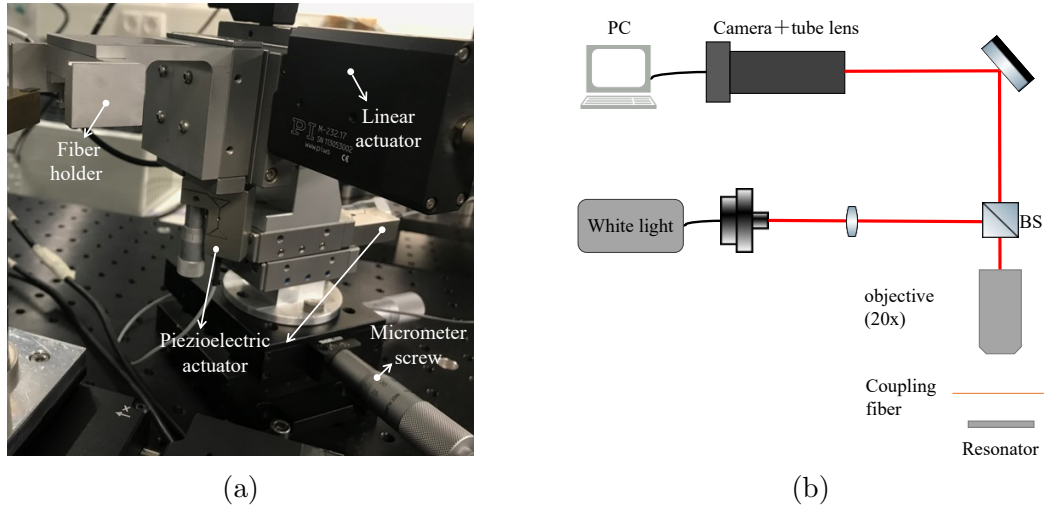


Figure 17: (a) A picture of the nanofiber positioning system. (b) Schematic of the built-up imaging system consisting of a 20x long working distance objective and a CMOS camera with white light for illumination.

**Position control of the sample** The sample can be moved in 3 directions by means of three orthogonally oriented positioning controls that consist of a 3-axis stage (Thorlabs, MAX303 NanoMax) driven by stepper motors (Physik Instrumente, M-232) allowing for a 4 mm travel range and a resolution of  $1\ \mu\text{m}$ .

**Imaging system** An objective (Mitutoyo, M Plan Apo 20x) combined with a CMOS camera (Allied Vision Technolgy, Marlin F131B ASG) is used to monitor the relative positioning of both the nanofiber and the resonator. The schematic of the imaging system is shown in Figure 17(b). The objective's 30.5 mm working distance allows for flexible placement when studying the characteristics of the resonator as well as changing the sample of interest.

### 3.2 Optical nanofiber

In this thesis, the light coupling is achieved by using an optical nanofiber fabricated from a commercial step-index single-mode glass fiber by tapering

the standard fiber down to subwavelength diameter using a heat-and-pull technique [45]. As illustrated in Figure 18, these glass fibers consist of a core with refractive index  $n_{\text{core}}$  and a cladding with refractive index  $n_{\text{clad}}$  which is slightly lower than  $n_{\text{core}}$ . The subwavelength nanofiber waist is connected by the two tapers on both sides which efficiently transfer the guided mode from the standard part of the fiber to the nanofiber waist by precise control of the taper geometry [46].

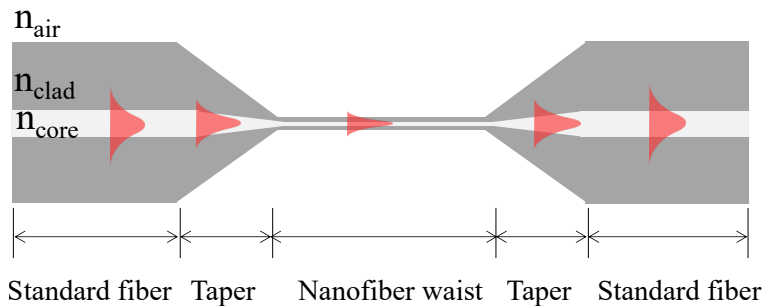


Figure 18: Sketch of an optical nanofiber, with nanofiber waist in between two tapered ends. In the standard part of the fiber, light is well confined into the core and guided by continuous total internal reflection due to the refractive index contrast between the core and the cladding. In the nanofiber waist, the total internal reflection occurs at the interface of the cladding and the surrounding medium (air) with refractive index  $n_{\text{air}}$ .

In [47] the mode propagation in step-index circular waveguides is described. In this general analysis, a structure (fiber) is assumed to be cylindrically symmetric along  $z$ , with radius  $a$  and refractive index  $n_1$ , surrounded by a medium with lower refractive index  $n_2$  that  $n_2 < n_1$ . In the modes analysis of cylindrical fiber, the first is to rewrite the Helmholtz equation in cylindrical coordinates in which the solutions give the  $z$ -components of electric and magnetic fields of the fiber. The other field components are derived from  $z$ -components using Maxwell's equations. For modes which propagate with propagation constant  $\beta$  along  $z$ , the ansatz in cylindrical coordinates has the form:

$$\begin{aligned} E_z &= R(r)\Phi(\varphi)Z(z) = E(r, \varphi)e^{j(\beta z - \omega t)} \\ H_z &= R(r)\Phi(\varphi)Z(z) = H(r, \varphi)e^{j(\beta z - \omega t)} \end{aligned} \quad (3.1)$$

Inserting Equation (3.1) into the Helmholtz yields:

$$\left(\frac{\partial^2}{\partial r^2} + \frac{1}{r} \frac{\partial}{\partial r} + \frac{1}{r^2} \frac{\partial^2}{\partial \varphi^2} + k_0^2 n^2 - \beta^2\right) \begin{pmatrix} E_z \\ H_z \end{pmatrix} = 0 \quad (3.2)$$

where  $n$  is the refractive index of the media. And  $\Phi(\varphi)$  has the form:

$$\Phi(\varphi) = C e^{j\nu\varphi} \quad (3.3)$$

where  $C$  is a constant and since circular symmetry requires  $\Phi(\varphi) = \Phi(\varphi + 2\pi)$ ,  $\nu$  must be an integer. And the term  $\nu$  is called the separation constant. Substituting Equation (3.1) and (3.3) into Equation (3.2) leads to an equation that only contains  $R(r)$ :

$$r^2 \frac{\partial^2 R}{\partial r^2} + r \frac{\partial R}{\partial r} + r^2 \left(k_0^2 n^2 - \beta^2 - \frac{\nu^2}{r^2}\right) R = 0 \quad (3.4)$$

The solutions to this differential equation are given by Bessel functions [47]. Bessel functions of the first kind of order  $\nu$ , symbolized by  $J_\nu(\kappa r)$ , are the solutions when the argument  $(k_0^2 n^2 - \beta^2 - \nu^2/r^2)$  is positive. Modified Bessel functions of the second kind of order  $\nu$ , symbolized by  $K_\nu(\gamma r)$ , are the solutions when the argument  $(k_0^2 n^2 - \beta^2 - \nu^2/r^2)$  is negative.  $\kappa$  and  $\gamma$  are defined as:

$$\begin{aligned} \kappa^2 &= k_0^2 n_1^2 - \beta^2 \quad (r \leq a) \\ \gamma^2 &= \beta^2 - k_0^2 n_2^2 \quad (r > a) \end{aligned} \quad (3.5)$$

As a result, the solutions of Equation (3.2) in both core and cladding are written as:

$$\begin{aligned} E_z &= \begin{cases} \frac{A}{J_\nu(U)} J_\nu\left(\frac{U}{a}r\right) e^{i\nu\varphi} & (r \leq a) \\ \frac{C}{K_\nu(W)} K_\nu\left(\frac{W}{a}r\right) e^{i\nu\varphi} & (r > a) \end{cases} \\ H_z &= \begin{cases} \frac{B}{J_\nu(U)} J_\nu\left(\frac{U}{a}r\right) e^{i\nu\varphi} & (r \leq a) \\ \frac{D}{K_\nu(W)} K_\nu\left(\frac{W}{a}r\right) e^{i\nu\varphi} & (r > a) \end{cases} \end{aligned} \quad (3.6)$$

where  $U = a\sqrt{k_0^2 n_1^2 - \beta^2}$  is the normalized propagation constant within the core ( $r \leq a$ ), and  $W$  is defined as  $W = a\sqrt{k_0^2 n_2^2 - \beta^2}$ . The coefficients A, B, C, and D are derived from the boundary conditions of the fields at the core-cladding interface, leading to the characteristic equation of the step-index fiber:

$$\begin{aligned} & \left[ \frac{J'_v(U)}{U J_v(U)} + \frac{K'_v(W)}{W K_v(W)} \right] \left[ n_1^2 \frac{J'_v(U)}{U J_v(U)} + n_2^2 \frac{K'_v(W)}{W K_v(W)} \right] \\ & = \left( \frac{v\beta}{k_0} \right)^2 \left( \frac{V}{UW} \right)^4 = \left( \frac{v\beta}{k_0} \right)^2 \left( \frac{1}{U^2} + \frac{1}{W^2} \right)^2 \end{aligned} \quad (3.7)$$

For each value of  $v$ , this equation yields a set of propagation constants  $\beta_{v,m}$ , with  $v$  the radial mode number, and  $m$  the angular mode number. Both  $v$  and  $m$  are integers. The effective refractive index (effective mode index) is defined as  $n_{\text{eff}} = \beta/k_0$ . The range of values that  $n_{\text{eff}}$  can take is [48]:

$$n_1 \geq n_{\text{eff}} \geq n_2 \quad (3.8)$$

For  $\nu = 0$ , the allowed modes will be either TE modes denoted by  $\text{TE}_{0m}$  or TM modes denoted by  $\text{TM}_{0m}$ . The only non-vanishing components of  $\text{TE}_{0m}$  modes are  $H_r, H_z$  and  $E_\varphi$ , whereas  $\text{TM}_{0m}$  modes only consist of  $E_r, E_z$  and  $H_\varphi$ . The characteristic equation for TE modes and TM modes simplifies to:

$$\begin{aligned} \frac{1}{U} \frac{J'_0(U)}{J_0(U)} + \frac{1}{W} \frac{K'_0(W)}{K_0(W)} &= 0 \quad (TE) \\ \frac{n_1^2}{U} \frac{J'_0(U)}{J_0(U)} + \frac{n_2^2}{W} \frac{K'_0(W)}{K_0(W)} &= 0 \quad (TM) \end{aligned} \quad (3.9)$$

For  $\nu \neq 0$ , the characteristic equation is more complicated to solve. The values of  $\beta$  will correspond to the modes containing both  $E_z$  and  $H_z$ , and therefore with six non-zero field components. These modes are called ‘‘hybrid modes’’, denoted by  $\text{EH}_{vm}$  and  $\text{HE}_{vm}$ , depending on the relative magnitude of  $E_z$  and  $H_z$ .

These general solutions apply to both the standard step-index fiber as well as the nanofiber waist. For the nanofiber waist, the mode is guided by the cladding-air interface, which can be again considered as a step-index fiber. By choosing a sufficiently small taper angle, the fundamental mode in the standard fiber part can be transformed adiabatically into the fundamental  $\text{HE}_{11}$  mode of the nanofiber. Figure 19(a) shows the numerical calculation of the effective mode index  $n_{\text{eff}}$  of  $\text{HE}_{11}$  mode in the nanofiber waist of glass fiber, giving the value  $n_{\text{eff}} = 1.1718$ . The evanescent field beyond the nanofiber surface decays at a length scale of a few hundred nanometers, allowing for evanescent coupling. This mode analysis wavelength is  $\lambda_0 = 785 \text{ nm}$ .

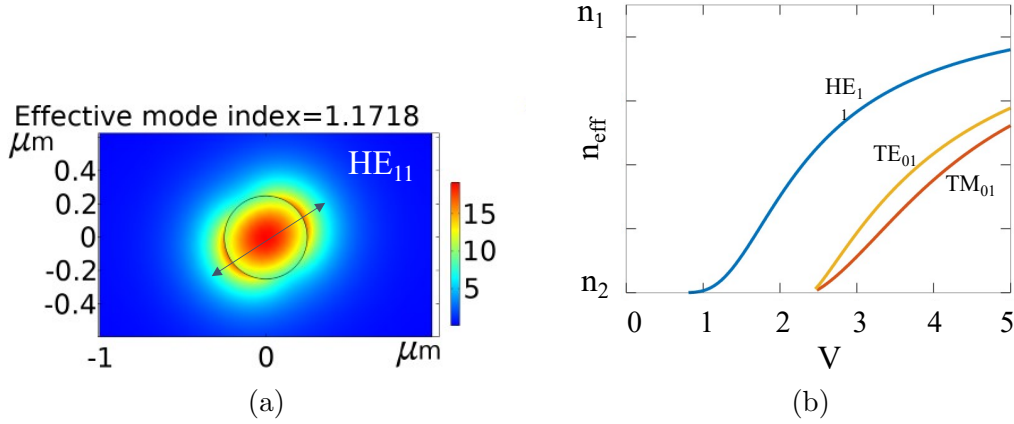


Figure 19: (a) Numerical calculation of the effective mode index of the fundamental mode HE<sub>11</sub> in the nanofiber waist (500 nm diameter) yields  $n_{\text{eff}} = 1.1718$  for a wavelength  $\lambda_0 = 785$  nm. The arrow indicates the polarization axis. (b) The effective refractive index  $n_{\text{eff}} = \beta/k_0$  as a function of the  $V$ -parameter for the fundamental HE<sub>11</sub> mode and the higher order modes TE<sub>01</sub> mode and TM<sub>01</sub> mode in a 500 nm diameter glass nanofiber. The first higher order modes, TE<sub>01</sub> mode and TM<sub>01</sub> mode can only be guided if the fiber radius is larger than a given cutoff radius  $a_{\text{cutoff}}$  for a given wavelength, while HE<sub>11</sub> mode exists for all fiber radii.

The electric field distribution at the radius of the nanofiber waist shows that the center of the nanofiber has the maximum intensity, and the evanescent field intensity outside the nanofiber is nearly as high as that within the nanofiber (see Figure 20). The mode has a discontinuity at the nanofiber's surface that is strongest pronounced along the polarization axis.

It is useful to introduce the normalized frequency  $V$  or  $V$ -parameter, defined as:

$$V = k_0 a_{\text{cutoff}} \sqrt{n_{\text{cladding}}^2 - n_{\text{air}}^2} \quad (3.10)$$

with the wave number  $k_0 = 2\pi/\lambda_0$ , and the radius  $a$ , the cutoff radius  $a_{\text{cutoff}}$  can be calculated from the condition  $V = 2.405$ .

Figure 19(b) plots the effective refractive index  $n_{\text{eff}}$  as a function of the normalized frequency  $V$  for HE<sub>11</sub> mode, TE<sub>01</sub> mode and TM<sub>01</sub> mode in a 500 nm diameter glass nanofiber. The  $V$ -parameter determines the number of modes in a fiber depending on the fiber diameter and optical wavelength and refractive indices. HE<sub>11</sub> is the fundamental mode, the only mode that is

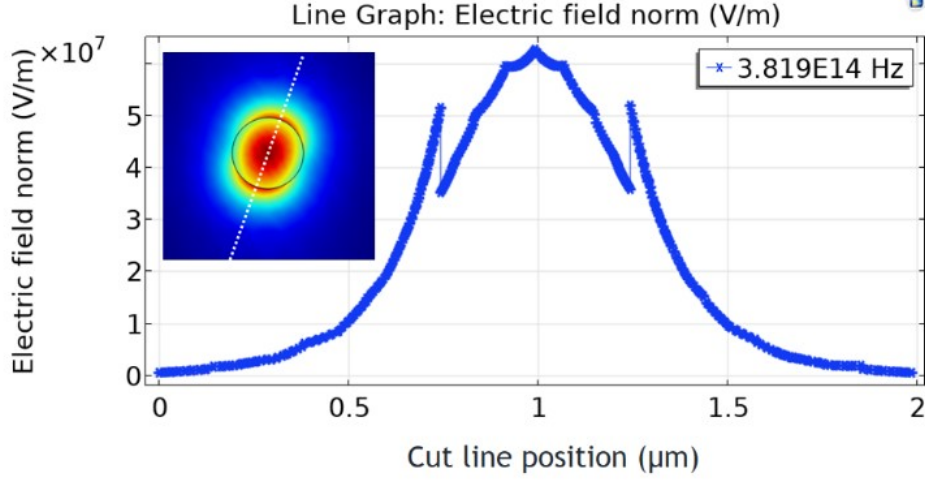


Figure 20: Electric field profile versus cut line (white dash line along the polarization axis) position. The evanescent field strength outside the nanofiber is nearly as high as that within the nanofiber.

guided for all fiber radii  $a$  with no cut-off value. The effective refractive index depends strongly on the  $V$ -parameter and as the  $V$ -parameter decreases, the fraction of the light propagating in the air increases. Therefore, the effective refractive index  $n_{\text{eff}}$  approaches  $n_2$  near the cut-off value [49], as shown in Figure 19(b).

For the first higher order modes  $\text{TE}_{01}$  and  $\text{TM}_{01}$ , the effective refractive index  $n_{\text{eff}}$  reaches the value  $n_2$  of the optically thinner medium at  $V = 2.405$ . That is,  $\text{TE}_{01}$  mode and  $\text{TM}_{01}$  mode can only be guided if the fiber radius is larger than a certain cutoff radius for a given wavelength. As a consequence, the single-mode condition of a fiber is  $V < 2.405$ . For the guided light with a wavelength  $\lambda_0 = 785$  nm, the cutoff radius of nanofiber's fundamental mode is calculated to be 286 nm, which means that with the radii less than this value, only the fundamental mode can be guided. For the nanofiber used in this experiment, the diameter  $a = 250$  nm  $<$  286 nm, so only  $\text{HE}_{11}$  mode is guided. Figure 20 is the plot of the electric field profile at the nanofiber waist cross-section, showing that the evanescent field strength outside the nanofiber is nearly as high as that within the nanofiber.

### 3.3 Sample layout

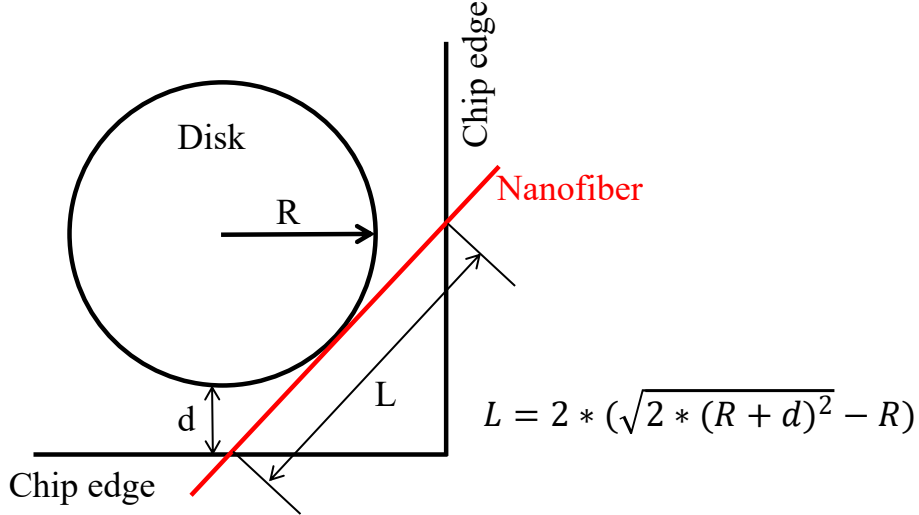


Figure 21: Sketch of the sample (top view) showing the relation between the microdisk radius ( $R$ ), its relative position to the chip edge ( $d$ ), and the length ( $L$ ) of the portion of nanofiber that crosses the substrate in order to couple light in and out from the microresonator.

The layout of the sample is designed according to our experimental needs and considering the lack of control in the tilt angle of the nanofiber mount. Specifically, in order to couple light from a nanofiber to the microresonator, it is fundamental to prevent the nanofiber from touching the substrate while approaching the microdisk. This can be done by minimizing the nanofiber length required to cross the chip in order to reach the target disk. In our case, this is accomplished by placing the target resonator as close to the chip's corner as possible and moving the nanofiber at  $45^\circ$  as shown in Figure 21. With this geometry, the length  $L$  of the nanofiber crossing the substrate to reach a disk with radius  $R$  at a distance  $d$  away from the chip edges is given by  $L = 2 \left( \sqrt{2(R + d)^2} - R \right)$ . Using the relation between nanofiber length  $L$  and the height of disks  $h$ , the maximum permitted tilt angle  $\theta$  (in degree) between the substrate and the nanofiber can be determined as  $\theta = \frac{180}{\pi} \cdot \arctan \left( \frac{2h}{L} \right)$ .

Two designs have been tested in this thesis. One is depicted in Figure 22(a), where the resonators are fabricated at a distance of roughly  $300 \mu\text{m}$  to prevent damage during the sample handling. In this case, the maximum allowed tilt

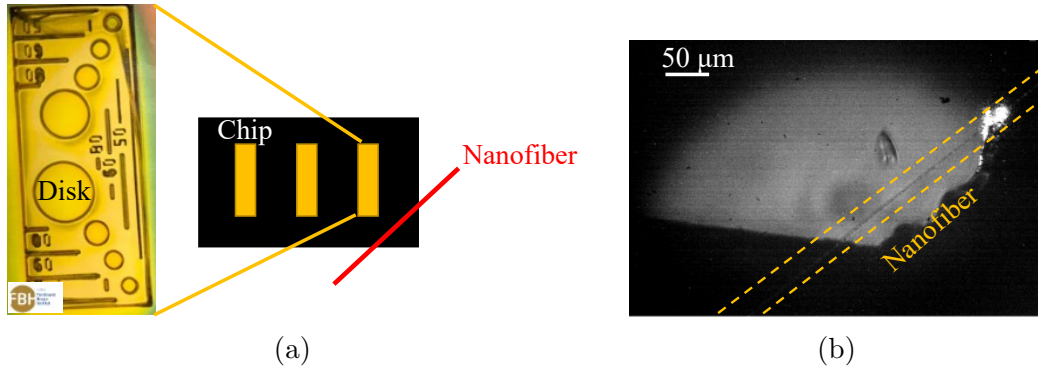


Figure 22: (a) Schematic of a chip design with the disk pattern marked in yellow and substrate marked in black. The nanofiber marked in red is placed at  $45^\circ$  with respect to the chip. (b) Image of the chip's corner, where the nanofiber touches the substrate at the edge of the chip before reaching the target resonator. This is visualized as scattered light at the chip edge and as a significant drop in the transmitted power of the nanofiber.

angle between substrate and nanofiber is  $0.7^\circ$ , assuming a disk height of  $6 \mu\text{m}$ . Figure 22(b) shows that with this design, the nanofiber gets in contact with the substrate, where one can observe a bright spot corresponding to scattered light at the contact point.

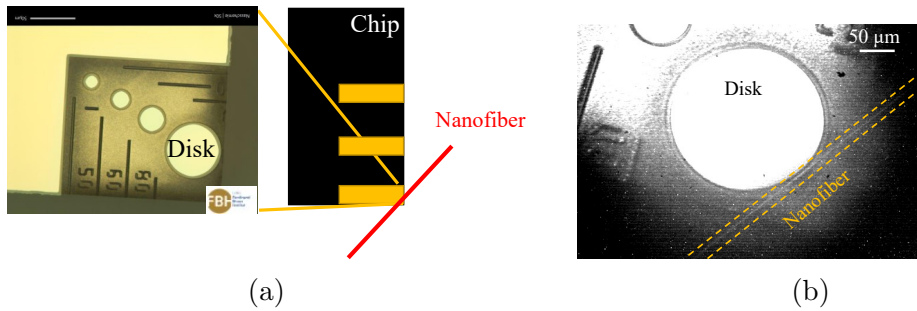


Figure 23: (a) Optical micrograph of the disk resonators at the lower-right corner of the chip. There are multiple resonators located diagonally with different diameters. (b) Image of the  $200 \mu\text{m}$  diameter disk resonator and the nanofiber (position indicated by the yellow dashed lines).

The second chip design is sketched in Figure 23(a). Here the resonators are located right at the chip's corner. On the diagonal of this pattern, there are disks with different diameters ranging from  $50 \mu\text{m}$  to  $200 \mu\text{m}$ . The shortest distance from disk to edge falls between  $10 \mu\text{m}$  to  $20 \mu\text{m}$ , resulting in a

maximum permitted tilted angle between substrate and the nanofiber of  $6^\circ$ , considering a disk height of  $6\ \mu\text{m}$ . Figure 23(b) shows that this chip design allows the nanofiber to reach a  $200\ \mu\text{m}$  diameter resonator without getting in contact with the substrate.

Q-factor measurements discussed in the next chapter are performed on samples with this second design, specifically on  $200\ \mu\text{m}$  diameter disk resonators with different thicknesses.

## 4 Results and discussion

### 4.1 A bottle resonator as a reference sample

As discussed in Chapter 1, the Q-factor of a resonator can be measured in the frequency domain from the FWHM linewidth  $\Delta\nu$  of the Lorentzian-shaped resonance dip using Equation (1.4) and (1.27).

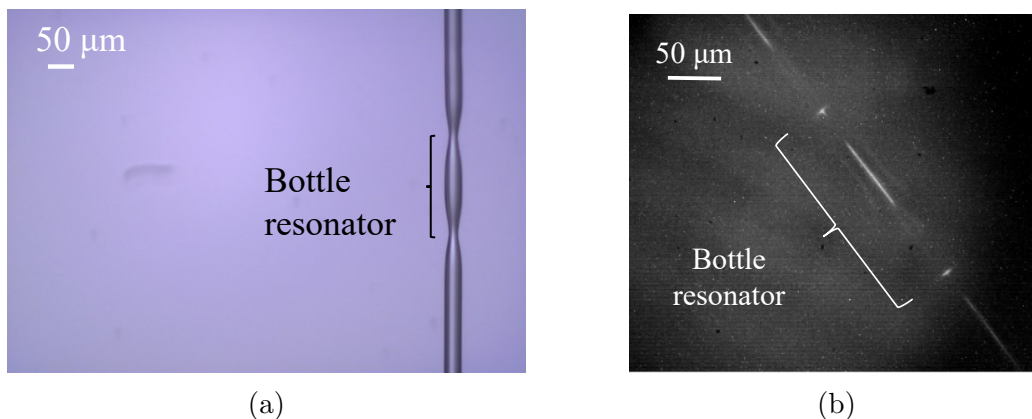


Figure 24: (a) Micrograph image of the bottle resonator. (b) Image of the bottle resonator taken from the imaging system sketched in Figure 17(b).

To test the performance of the experimental setup described in Chapter 3, a Q-factor measurement is first performed on a reference sample made of a glass bottle resonator with expected intrinsic Q-factor between  $10^6 - 10^8$  depending on the bottle diameter [13].

The bottle resonator is fabricated in our lab using the flame-brush technique described in [50] and it exhibits a parabolic fiber diameter variation (from 12  $\mu\text{m}$  to 29  $\mu\text{m}$ ), as shown in Figure 24(a).

Figure 24(b) shows the 29  $\mu\text{m}$ -bottle resonator as imaged in the setup sketched in Figure 17(b), with the resonator region positioned between two micro tapers.

In order to excite the resonator's modes, a linear and symmetric ramp voltage is sent to the laser driver to generate a frequency scan over 1 THz (almost the

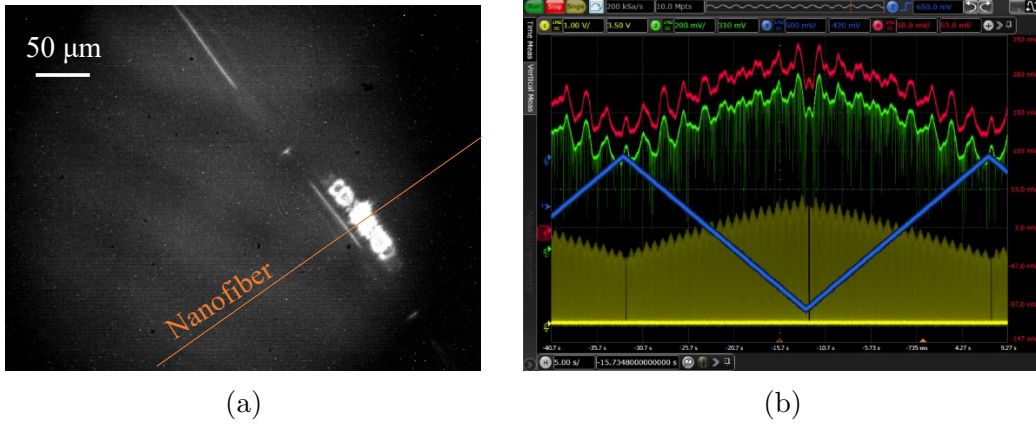


Figure 25: (a) Image of the bottle modes visualized by the scattered light when the nanofiber and resonator are in contact. (b) Display of digital oscilloscope used to capture the signals for Q-factor measurement. The excitation of different resonant modes in the bottle resonator leads to drops in the nanofiber transmission (green signal).

full scanning range of the DFB laser) while the nanofiber-resonator distance is varied with the stepper motors and the piezoelectric screws.

Resonances can be qualitatively observed with the imaging system (Figure 25(a)) or quantitatively analyzed by monitoring the nanofiber transmission spectrum, as shown in Figure 25(b). Here, the blue signal represents the ramp voltage, the yellow signal comes from the Fabry-Pérot cavity and shows consecutive peaks separated by 1.5 GHz, and the green signal is the transmission of the nanofiber. The red signal monitors the laser's power fluctuation during the frequency scan and normalizes the nanofiber power transmission.

To determine the intrinsic Q-factor, a critically-coupled regime needs to be reached. This is done by continuously scanning the laser frequency around a resonance while monitoring the depth of the resonance dips by adjusting the nanofiber-bottle distance and the polarization of the input light. As discussed in Chapter 1, the depth of the resonance dips reaches its maximum in the critically-coupled regime: experimentally this is shown in Figure 26. Let us note that the minimum transmission is larger than 0. This could be due to a polarization mismatch between the mode supported by the nanofiber and that of the bottle resonator. The black curve is the normalized transmission that is normalized by the 10% of the power going directly to the photodiode after passing through the fiber beam splitter. The red curve is the Lorentzian

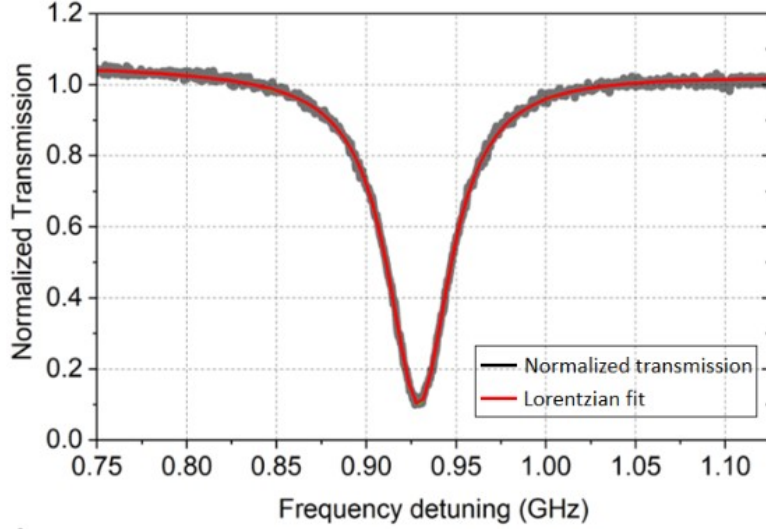


Figure 26: Transmission profile of a 29  $\mu\text{m}$  glass bottle resonator in critically-coupled regime. The red solid curve is the Lorentzian fit which gives a linewidth of  $\Delta\nu = (42.2 \pm 0.1)$  MHz and a minimum normalized transmission of  $(0.060 \pm 0.002)$ . The corresponding intrinsic Q-factor is calculated to be  $(1.811 \pm 0.004) \times 10^7$ , according to Equation (1.28).

fit which gives a linewidth of  $\Delta\nu = (42.2 \pm 0.1)$  MHz and a minimum normalized transmission at the resonance of  $(0.060 \pm 0.002)$ . The corresponding intrinsic Q-factor is then calculated to be  $(1.811 \pm 0.004) \times 10^7$  using Equation (1.28), which falls in the range of the expected intrinsic Q-factors of  $10^6 - 10^8$ .

## 4.2 Q-factor measurement of microdisk resonators

Figure 27 is a picture of the working experimental setup containing both the nanofiber (position indicated by the red line) and resonator chip holder with the nanofiber mounted at  $45^\circ$  with respect to the chip, according to the discussion presented in Section 3.3.

At first, a 200  $\mu\text{m}$ -diameter large and 813 nm thick microdisk is characterized. According to Equation 1.2, the expected FSR is 318 GHz. In a frequency scan of about 1.5 FSR one can see several resonance dips, as shown in Figure 28. Calculating the frequency spacing between the same dips labeled as 1, 2, 3 gives an averaged FSR of  $(326 \pm 3)$  GHz, corresponding to a disk radius of

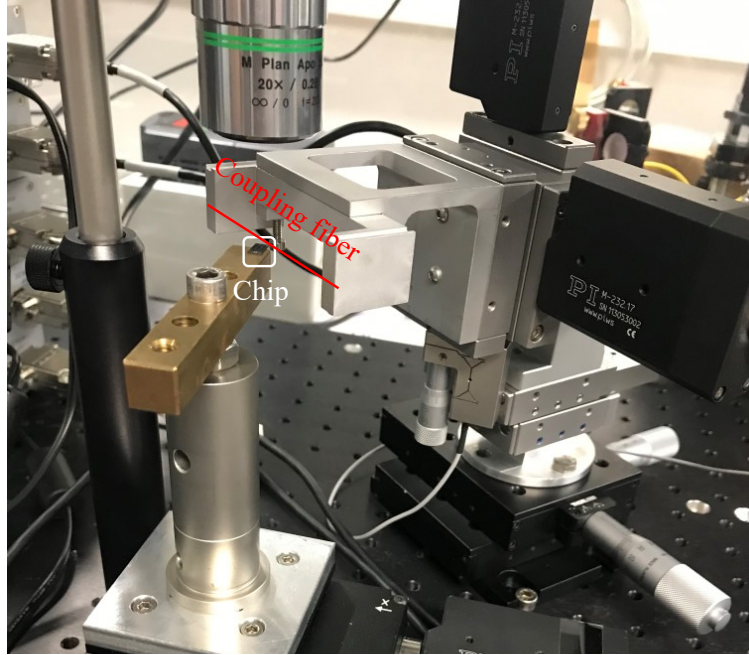


Figure 27: Picture of the working experimental setup. The nanofiber indicated by the red line, is mounted at  $45^\circ$  with respect to the resonator chip. The nanofiber and chip holders can be moved independently using the positioning systems. A 20X objective with 35 mm working distance provides a top view of both components allowing to monitor their relative position in real-time.

$(97.5 \pm 0.3) \mu\text{m}$ . Changing the nanofiber-resonator distance did not lead to a perfect critically-coupled regime (i.e.  $T = 0$ ). Fitting the resonance dip for the case with minimum transmission provides a loaded Q-factor  $\sim 10^5$

The second measurement is performed on a  $200 \mu\text{m}$ -diameter large and  $461 \text{ nm}$  thick microdisk. The laser frequency is tuned over a range bigger than the expected FSR of  $318 \text{ GHz}$ , in order to find the resonant modes with certainty. Specifically, the laser frequency is continuously scanned over  $957.6 \text{ GHz}$  forwardly and backwardly, by applying a periodic and symmetric ramp voltage generated by an external waveform generator to the laser temperature controller. As expected, within this scanning range (highlighted by the voltage ramp shown in green in the graph in Figure 29), three resonance dips can be observed (labeled as 1, 2, and 3) in the nanofiber transmission (black curve in Figure 29). The average value of the relative distance of the dips yields a measured FSR of  $(316.76 \pm 0.01) \text{ GHz}$ , which corresponds to a disk radius of  $(100.4 \pm 0.8) \mu\text{m}$ .

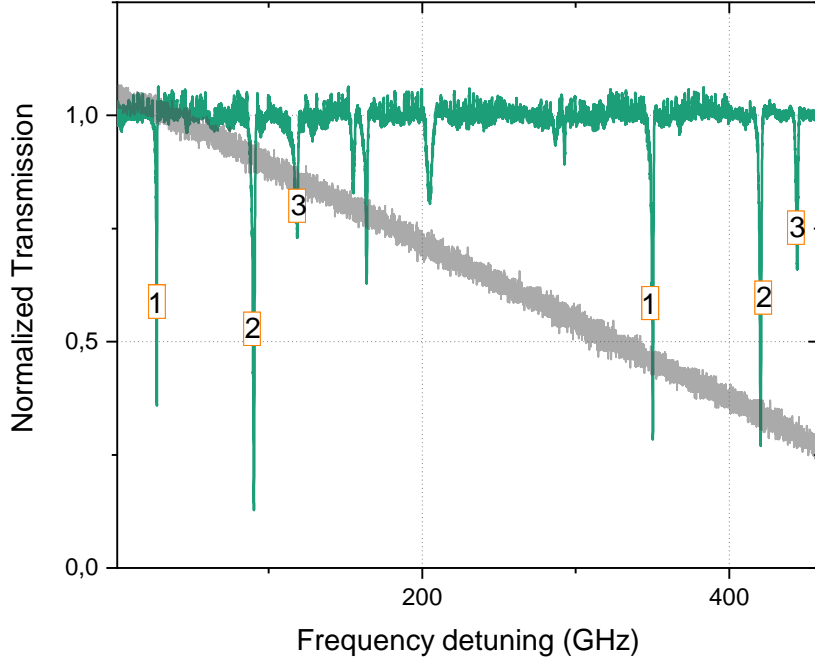


Figure 28: Transmission of the nanofiber (green line) versus laser frequency detuning by applying a linear voltage ramp (gray line) to the laser temperature controller. In about 1.5 FSR, several dips are observed. The averaged relative distance of the dips (labeled as 1, 2, 3) is calculated to be equal to  $(326 \pm 3)$  GHz, corresponding to the expected FSR for a 200  $\mu\text{m}$  diameter disk.

The comparison of linewidths under forward and backward frequency scan is essential to see if there were unwanted thermo-optic effects introduced by the pump power. In fact, when the pump power is sufficiently low, the resonance dip should have an approximate ideal Lorentzian shape. For increasing power, instead, the shape of the resonance dip would become asymmetric and deformed [51]. This is due to the fact that when the resonator heats up, its resonances shift towards lower frequency and the response transmission linewidths obtained under forward and backward frequency scan are different. In the forward frequency scan, the non-linear frequency shift pushes the resonance away from the probe laser resulting in resonance broadening. In the backward frequency scan, the resonance is dragged towards the probe laser leading to a resonance that is narrower than that in the linear

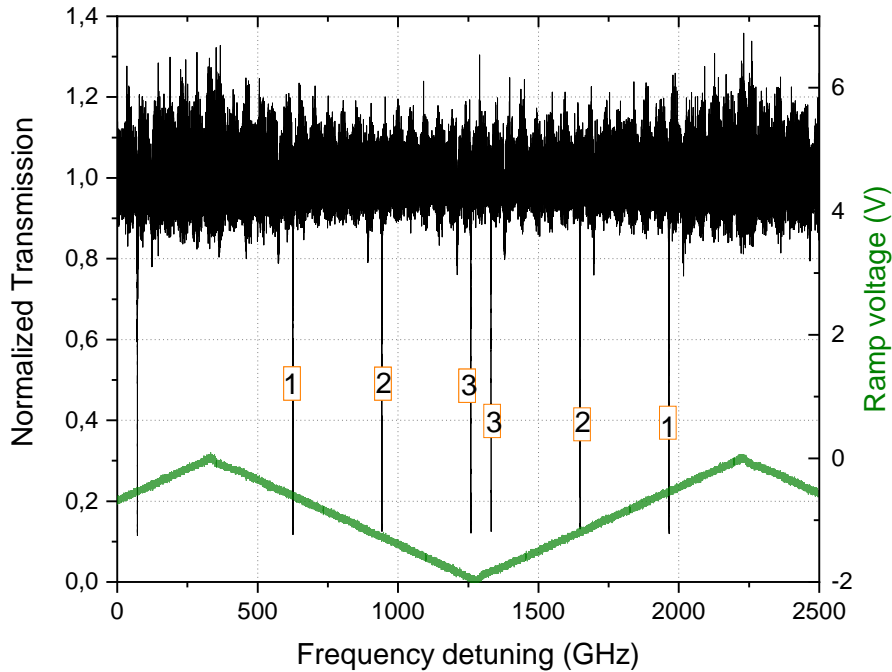
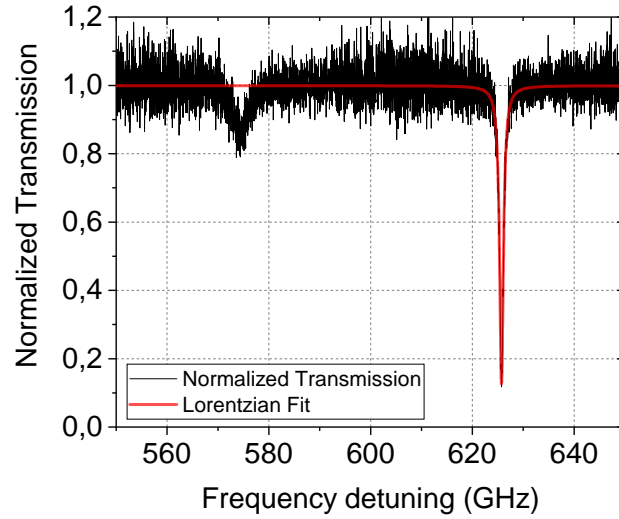


Figure 29: Transmission of the nanofiber (black line) over time while tuning the frequency of the input laser over 957.6 GHz by applying a linear voltage ramp (green line) to the laser temperature controller. Three dips are observed within each ramp and are labeled as 1, 2, and 3. The averaged distance of the dips is calculated to be equal to  $(316.76 \pm 0.01)$  GHz, corresponding to the expected FSR for a 200  $\mu\text{m}$  diameter disk, therefore proving that the 3 dips, in fact, correspond to the same resonant mode.

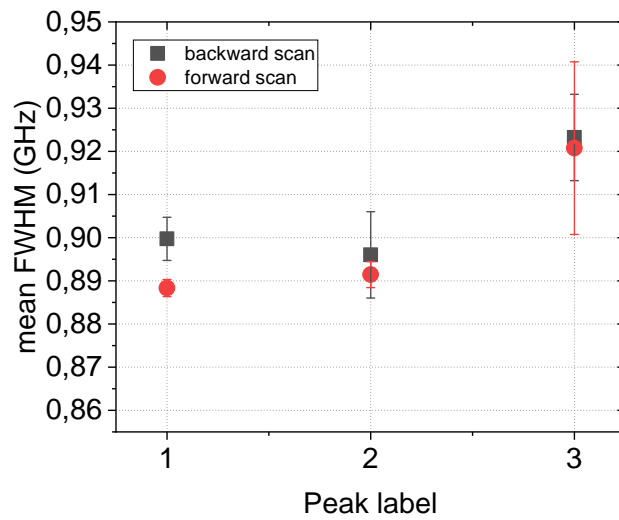
regime [52]. As a result of the broadening or compression of the resonance dip generated by thermo-optic effects, the Q-factor might be underestimated or overestimated, respectively.

With a power of 0.27  $\mu\text{W}$  into the nanofiber, the main resonance dip looks symmetric and is well described by a Lorentzian curve (see 30(a)). This is also confirmed by repeating the same measurement over 3 FSR and several forward and backward scans. Figure 30(b) plots the averaged FWHM (error bar is the maximum deviation) for the three dips, which are all consistent with one another.

To finally reach critical coupling, the frequency scanning range is narrowed



(a)



(b)

Figure 30: (a) Zoom-in on one of the resonance dips in Figure 29. (b) Graph compares the mean FWHM of resonance dips labeled 1, 2, and 3 under the forward and backward frequency scans. With a power of  $0.27 \mu\text{W}$  in the nanofiber, no thermo-optic effects are introduced since the dip is symmetric and with comparable mean values for forward and backward frequency scans.

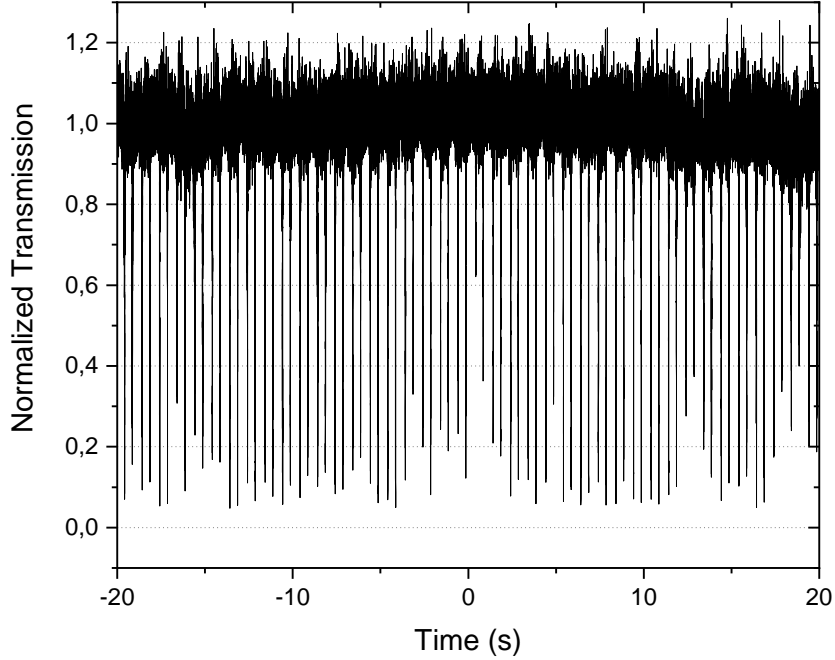
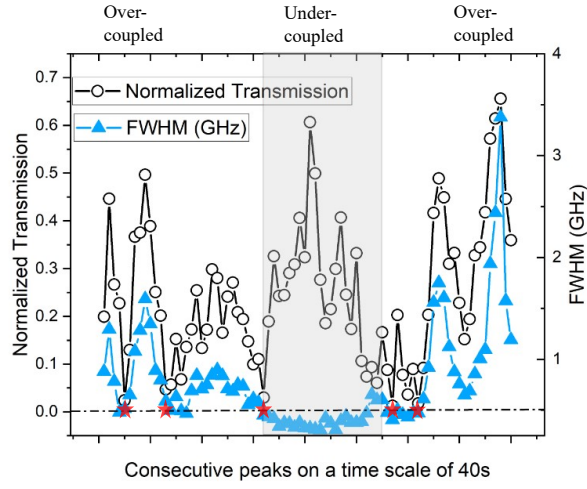


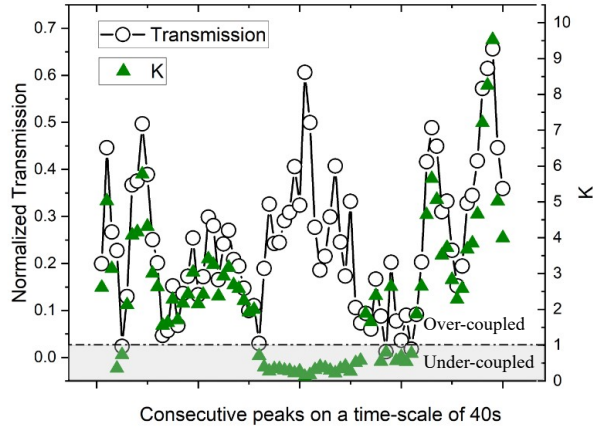
Figure 31: Consecutive resonance dips in 40 frequency scanning periods. The fluctuation in the depth of the transmission indicates that there exist variations in the distance between the nanofiber and the resonator during the time scale of several frequency scanning periods.

down to focus on only one resonance dip in a single scanning period: in this case, with a 39.9 GHz range in both forward and backward scans. While continuously repeating the frequency scan, a notable fluctuation in the depth of the resonance dip was observed in the transmission signal without intentionally changing the nanofiber-resonator distance. This fluctuation is due to the position of the nanofiber shifts during the measurement (in this case, likely induced by some residual air flow), resulting in random variation over time of nanofiber-resonator distance. However, the collection of the same dip over several tens of frequency scanning periods can be used to identify different coupling regimes.

As previously described in Section 1.3, the transmission reduces as the FWHM gets broader when the nanofiber moves from under-coupled to the critically-coupled regime and achieves the minimum value (ideally 0) of transmission



(a)



(b)

Figure 32: (a) Plot of transmission and FWHM of each subsequent resonance dip in Figure 31, indicates the transitions among different coupling regimes. The nanofiber is in the under-coupled regime at points with high transmission and a relatively smaller FWHM. Points with high transmission and a relatively larger FWHM are in the over-coupled regime. The transition points between different regimes give the candidates of the critically-coupled points marked with red stars. (b) Plot of transmission and  $K$ , which provides a different method to identify the critically-coupled regime by  $K = 1$ , under-coupled by  $K < 1$ , and over-coupled by  $K > 1$ .

in the critically-coupled regime. While the nanofiber goes from critically-coupled to over-coupled regime, the transmission recovers and the FWHM gets even broader. By doing a Lorentzian fit to each subsequent resonance dip, the behavior of both the FWHM and transmission offers a method to plot the transmission among the different coupling regimes as shown in Figure 32(a). The transition points between different regimes give the candidates of the critically-coupled points.

Alternatively, one can calculate the coupling parameter  $K$  by the transmission of each resonance dip according to Equation (1.29). In Figure 32(b), transition among different coupling regimes is observed:  $K = 1$  represents the critically coupled regime,  $K < 1$  and  $K > 1$  are the under-coupled regime and over-coupled regime, respectively.

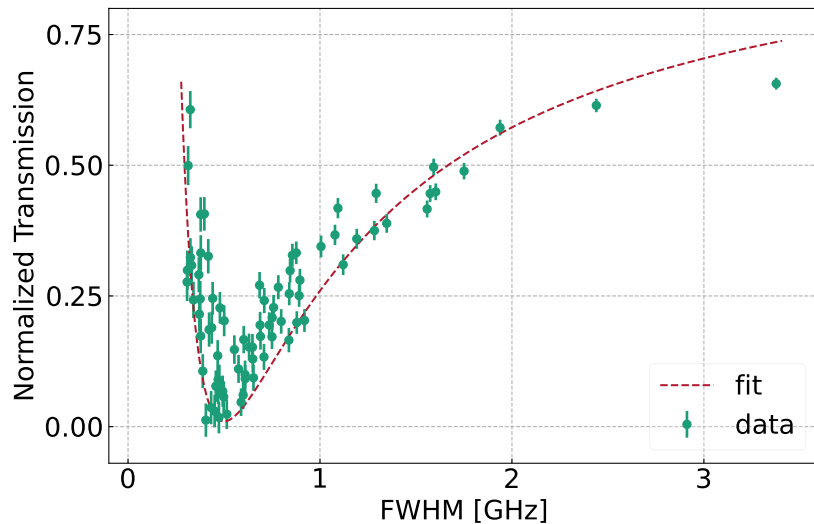


Figure 33: Transmission as a function of the resonance linewidth (FWHM) in different coupling regimes. The solid line is calculated by Equation (4.1) using the coupling model in Figure 4. The fitting curve gives the value of  $\tau_0^{-1} = (1.57 \pm 0.01)$  GHz, corresponding to an intrinsic Q-factor of  $(1.53 \pm 0.02) \times 10^6$ .

The transition among different regimes in Figure 32(a) and (b) can finally be used to estimate the intrinsic Q-factor, as shown in Figure 33. In this graph, the on-resonance transmission  $T_{res}$  of each resonance dip is plotted

versus the corresponding FWHM  $\Delta\nu_{\text{measured}}$ . The fitting model is derived by rewriting Equation (1.26) as  $T_{\text{res}}$  versus  $\Delta\nu_{\text{measured}}$ :

$$T_{\text{res}} = c + \left( \frac{\tau_e^{-1} - \tau_0^{-1}}{\tau_e^{-1} + \tau_0^{-1}} \right)^2 = c + \left( \frac{\Delta\nu_{\text{measured}} - \frac{1}{\pi}\tau_0^{-1}}{\Delta\nu_{\text{measured}}} \right)^2 \quad (4.1)$$

where  $2\pi\Delta\nu_{\text{measured}} = \tau_e^{-1} + \tau_0^{-1}$ , and  $c$  is a constant, which could, e.g., come from phase mismatch in the experiment [22].

The fitting curve (solid line) in Figure 33 is calculated by Equation (4.1) and this fitting curve gives the value of  $\tau_0^{-1} = (1.57 \pm 0.01)$  GHz. According to Equation (1.3) or (1.4), the intrinsic Q-factor is calculated to be  $(1.53 \pm 0.02) \times 10^6$ .

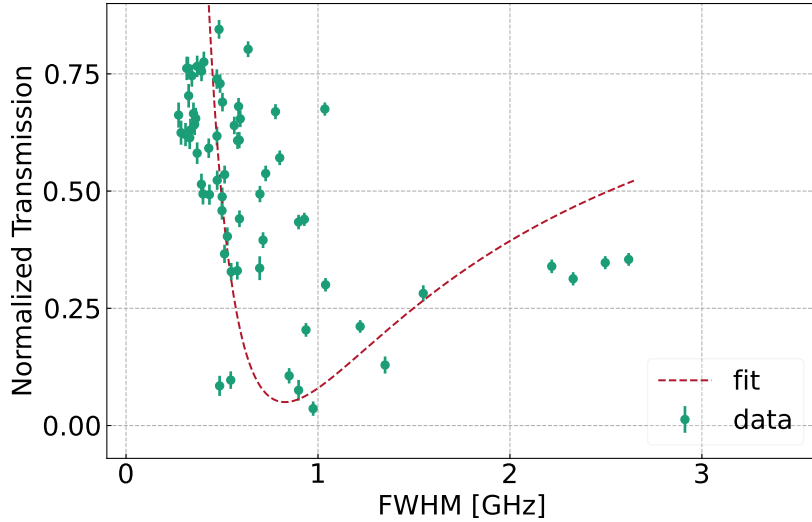


Figure 34: Microdisk resonator of 385 nm thickness: Transmission as a function of the linewidth (FWHM) of the resonance dips in different coupling regimes. The solid fitting curve gives the value of  $\tau_0^{-1} = (2.600 \pm 0.003)$  GHz, corresponding to an intrinsic Q-factor of  $(0.921 \pm 0.001) \times 10^6$ .

The same analysis is performed on a thinner 200  $\mu\text{m}$  diameter microdisk with a thickness of 385 nm. Figure 34 shows the plot of the on-resonance power transmission versus its resonance linewidth. The fitting curve gives the value of  $\tau_0^{-1} = (2.600 \pm 0.003)$  GHz. From this value, we infer the intrinsic Q-factor of this resonator to be  $(0.921 \pm 0.001) \times 10^6$ .

## 5 Summary and outlook

In this thesis, I established an experimental method to measure the intrinsic Q-factor of on-chip silica microdisk resonators in the frequency domain. The Q-factor measurement is based on the evanescent coupling between an optical nanofiber and the microresonator and the experimental setup implemented during this thesis allows one to adjust the nanofiber-resonator coupling efficiency by varying the nanofiber-resonator distance. The method consists in analyzing the power transmission spectrum of nanofiber while scanning the laser frequency and adjusting the nanofiber-resonator distance. The resonances of the microdisk are observed as Lorentzian dips in the transmission. The intrinsic Q-factor of the resonators was estimated subsequently by fitting the data with a waveguide-resonator coupling model. The Q-factor measurements were carried out on the 200  $\mu\text{m}$  diameter resonators with different thicknesses, the measured intrinsic Q-factor are as high as  $(1.53 \pm 0.02) \times 10^6$  (461 nm thick) and  $(0.921 \pm 0.001) \times 10^6$  (385 nm thick), respectively.

The setup developed during this thesis is capable of characterizing different types of WGM resonators by simply changing the sample holder. For example, fiber-based microresonators such as bottle resonators or microsphere resonators. As an outlook of this work, the mechanical stability could be improved by:

1. Lowering down the height of both sample and nanofiber holders/stages by using compact translation stages for both nanofiber and chips.
2. Adding tilt angle control to the nanofiber holder adjusting the tilt angle between the nanofiber and resonator, which enables the nanofiber to cross a larger area of the chip without unwanted contact with the substrate. This could be done for example, by attaching one end of the nanofiber to a bending piezoelectric actuator.
3. Using closed-loop piezoelectric screws instead of open-loops in the control of the positions. This would allow the acquisition of absolute nanofiber-resonator distance and lead to better performance on the nanofiber transmission versus nanofiber-resonator distance. This contributes to the concept of an integrated system that the resonators and the coupling waveguides are integrated into the chip, in which the positional characterization of the microresonators is taken into consideration.
4. Adding a translation stage for nanofiber stretch control to avoid possible nanofiber position shifts during light coupling.

Furthermore, the quality of the microdisk resonator samples could be improved by polishing the side surface to reduce the surface roughness which causes the surface-related losses.

## References

- [1] F. Vollmer and S. Arnold, *Whispering-gallery-mode biosensing: label-free detection down to single molecules*, [Nature methods](#) **5**, 591–596 (2008).
- [2] G. C. Righini and S. Soria, *Biosensing by WGM microspherical resonators*, [Sensors](#) **16**, 905 (2016).
- [3] C. Ciminelli, C. M. Campanella, F. Dell’Olio, C. E. Campanella, and M. N. Armenise, *Label-free optical resonant sensors for biochemical applications*, [Progress in Quantum electronics](#) **37**, 51–107 (2013).
- [4] J. Dionne, H. Ashwath, and L. Kuznetsova, *Subwavelength silicon disk whispering-gallery-mode microcavities for size-dependent nanoparticles detection in the mid-infrared*, [Optical Engineering](#) **56**, 057111–057111 (2017).
- [5] *Whispering-gallery mode microdisk lasers*, author=McCall, SL and Levi, AFJ and Slusher, RE and Pearton, SJ and Logan, RA, [Applied physics letters](#) **60**, 289–291 (1992).
- [6] W. Liang, V. Ilchenko, D. Eliyahu, A. Savchenkov, A. Matsko, D. Seidel, and L. Maleki, *Ultralow noise miniature external cavity semiconductor laser*, [Nature communications](#) **6**, 7371 (2015).
- [7] V. R. Almeida, C. A. Barrios, R. R. Panepucci, and M. Lipson, *All-optical control of light on a silicon chip*, [Nature](#) **431**, 1081–1084 (2004).
- [8] W. Bogaerts, P. De Heyn, T. Van Vaerenbergh, K. De Vos, S. Kumar Selvaraja, T. Claes, P. Dumon, P. Bienstman, D. Van Thourhout, and R. Baets, *Silicon microring resonators*, [Laser & Photonics Reviews](#) **6**, 47–73 (2012).
- [9] P. R. Berman, *Cavity quantum electrodynamics*, [Advances in atomic](#) (1994).
- [10] I. Oreshnikov and D. Skryabin, *Multiple nonlinear resonances and frequency combs in bottle microresonators*, [Optics express](#) **25**, 10306–10311 (2017).
- [11] M.-G. Suh, Q.-F. Yang, K. Y. Yang, X. Yi, and K. J. Vahala, *Microresonator soliton dual-comb spectroscopy*, [Science](#) **354**, 600–603 (2016).
- [12] N. R. Newbury, I. Coddington, and W. Swann, *Sensitivity of coherent dual-comb spectroscopy*, [Optics express](#) **18**, 7929–7945 (2010).
- [13] M. Pöllinger, *Bottle microresonators for applications in quantum optics and all-optical signal processing*, [Ph.D. thesis](#), Mainz, Univ., Diss., 2011 (2010).
- [14] Y. Chen, J. Li, X. Guo, L. Wan, J. Liu, Z. Chen, J. Pan, B. Zhang, Z. Li, and Y. Qin, *On-chip high-sensitivity photonic temperature sensor based on a GaAs microresonator*, [Optics Letters](#) **45**, 5105–5108 (2020).

- [15] J. Liao and L. Yang, *Optical whispering-gallery mode barcodes for high-precision and wide-range temperature measurements*, [Light: Science & Applications](#) **10**, 32 (2021).
- [16] J. M. Gamba, *The role of transport phenomena in whispering gallery mode optical biosensor performance*, [Ph.D. thesis](#), California Institute of Technology (2012).
- [17] F. Khozeymeh and M. Razaghi, *Cylindrical optical resonators: fundamental properties and bio-sensing characteristics*, [Journal of Optics](#) **20**, 045301 (2018).
- [18] F. Khozeymeh, M. Razaghi, T. Chalyan, and L. Pavesi, *Fast analytical modelling of an SOI micro-ring resonator for bio-sensing application*, [Journal of Physics D: Applied Physics](#) **51**, 285401 (2018).
- [19] L. Rayleigh, *CXII. The problem of the whispering gallery*, [The London, Edinburgh, and Dublin Philosophical Magazine and Journal of Science](#) **20**, 1001–1004 (1910).
- [20] A. Shitikov, I. Bilenko, N. Kondratiev, V. Lobanov, A. Markosyan, and M. Gorodetsky, *Billion Q-factor in silicon WGM resonators*, [Optica](#) **5**, 1525–1528 (2018).
- [21] A. Chiasera, Y. Dumeige, P. Feron, M. Ferrari, Y. Jestin, G. Nunzi Conti, S. Pelli, S. Soria, and G. C. Righini, *Spherical whispering-gallery-mode microresonators*, [Laser & Photonics Reviews](#) **4**, 457–482 (2010).
- [22] K. J. Vahala, *Optical microcavities*, [nature](#) **424**, 839–846 (2003).
- [23] B. E. A. Saleh and M. C. Teich, *Resonator Optics*, in [Fundamentals of Photonics](#) (John Wiley & Sons, Ltd, 1991) Chap. 9, pp. 310–341, <https://onlinelibrary.wiley.com/doi/pdf/10.1002/0471213748.ch9> .
- [24] D. Meschede, *Optics, light and lasers: the practical approach to modern aspects of photonics and laser physics* (John Wiley & Sons, 2017).
- [25] J. Ward and O. Benson, *WGM microresonators: sensing, lasing and fundamental optics with microspheres* (2011).
- [26] K. Srinivasan, M. Borselli, O. Painter, A. Stintz, and S. Krishna, *Cavity Q, mode volume, and lasing threshold in small diameter AlGaAs microdisks with embedded quantum dots*, [Optics express](#) **14**, 1094–1105 (2006).
- [27] G. Lin, A. Coillet, and Y. K. Chembo, *Nonlinear photonics with high-Q whispering-gallery-mode resonators*, [Advances in Optics and Photonics](#) **9**, 828–890 (2017).
- [28] M. Pöllinger, F. Warken, W. Alt, and D. Meschede, *A Tunable Whispering-Gallery-Mode Bottle Resonator*, in [The European Conference on Lasers and Electro-Optics](#) (Optica Publishing Group, 2007) p. JSP1.5.

- [29] D. A. Steck, *Classical and modern optics*, Oregon University (2006).
- [30] M. Qu and Z.-X. Huang, *Frustrated total internal reflection: resonant and negative Goos-Hänchen shifts in microwave regime*, *Optics Communications* **284**, 2604–2607 (2011).
- [31] G. A. Santamaría-Botello, L. G. Muñoz, F. Sedlmeir, S. Preu, D. Segovia-Vargas, K. A. Abdalmalak, S. L. Romano, A. G. Lampérez, S. Malzer, G. Döhler, *et al.*, *Maximization of the optical intra-cavity power of whispering-gallery mode resonators via coupling prism*, *Optics express* **24**, 26503–26514 (2016).
- [32] Y. A. Demchenko, I. A. Bilenko, and M. Gorodetsky, *Optimisation of the prism coupling of optical whispering-gallery-mode microcavities*, *Quantum Electronics* **47**, 743 (2017).
- [33] V. S. Ilchenko, X. S. Yao, and L. Maleki, *Pigtailing the high-Q microsphere cavity: a simple fiber coupler for optical whispering-gallery modes*, *Optics letters* **24**, 723–725 (1999).
- [34] V. S. Ilchenko and A. B. Matsko, *Optical resonators with whispering-gallery modes-part II: applications*, *IEEE Journal of selected topics in quantum electronics* **12**, 15–32 (2006).
- [35] S. Spillane, T. Kippenberg, O. Painter, and K. Vahala, *Ideality in a fiber-taper-coupled microresonator system for application to cavity quantum electrodynamics*, *Physical review letters* **91**, 043902 (2003).
- [36] S. M. Spillane, *Fiber-coupled Ultra-high-Q Microresonators for Nonlinear and Quantum Optics*, *Ph.D. thesis*, California Institute of Technology (2004).
- [37] H. A. Haus, *Waves and fields in optoelectronics* (Englewood Cliffs, NJ : Prentice-Hall, 1984).
- [38] G. C. Righini, Y. Dumeige, P. Feron, M. Ferrari, G. Nunzi Conti, D. Ristic, and S. Soria, *Whispering gallery mode microresonators: fundamentals and applications*, *La Rivista del Nuovo Cimento* **34**, 435–488 (2011).
- [39] Information provided by Dr. Andreas Thies and Jan. Schlegel, Process Technology, Ferdinand-Braun-Institut (FBH).
- [40] C. Dettmann, G. Morozov, M. Sieber, and H. Waalkens, *TM and TE directional modes of an optical microdisk resonator with a point scatterer*, in *2008 10th Anniversary International Conference on Transparent Optical Networks*, Vol. 4 (IEEE, 2008) pp. 65–68.
- [41] C. Junge, *Cavity quantum electrodynamics with non-transversal photons*, *Ph.D. thesis*, Technische Universität Wien (2013).
- [42] F. Ramiro-Manzano, N. Prtljaga, L. Pavesi, G. Pucker, and M. Ghulinyan, *A fully integrated high-Q whispering-gallery wedge resonator*, *Optics express* **20**, 22934–22942 (2012).

- [43] D. V. Strekalov, C. Marquardt, A. B. Matsko, H. G. Schwefel, and G. Leuchs, *Nonlinear and quantum optics with whispering gallery resonators*, [Journal of Optics](#) **18**, 123002 (2016).
- [44] M. L. Gorodetsky, A. D. Pryamikov, and V. S. Ilchenko, *Rayleigh scattering in high- $Q$  microspheres*, [JOSA B](#) **17**, 1051–1057 (2000).
- [45] C. Wuttke, *Thermal excitations of optical nanofibers measured with a fiber-integrated Fabry-Pérot cavity*, [Ph.D. thesis](#), Mainz, Univ., Diss., 2014 (2014).
- [46] S. Ravets, J. Hoffman, L. Orozco, S. Rolston, G. Beadie, and F. Fatemi, *A low-loss photonic silica nanofiber for higher-order modes*, [Optics express](#) **21**, 18325–18335 (2013).
- [47] C. Pollock and M. Lipson, *Integrated photonics*, Vol. 20 (Springer, 2003).
- [48] G. T. Reed and A. P. Knights, *Silicon photonics: an introduction* (John Wiley & Sons, 2004).
- [49] A. Stiebeiner, *Nanofiber-based spectroscopy of organic molecules*, [Ph.D. thesis](#), Mainz, Univ., Diss., 2014 (2014).
- [50] M. Pöllinger, D. O’Shea, F. Warcken, and A. Rauschenbeutel, *Ultrahigh- $Q$  tunable whispering-gallery-mode microresonator*, [Physical review letters](#) **103**, 053901 (2009).
- [51] J. Wang, B. Zhu, Z. Hao, F. Bo, X. Wang, F. Gao, Y. Li, G. Zhang, and J. Xu, *Thermo-optic effects in on-chip lithium niobate microdisk resonators*, [Optics Express](#) **24**, 21869–21879 (2016).
- [52] A. Rasoloniaina, V. Huet, M. Thual, S. Balac, P. Féron, and Y. Dumeige, *Analysis of third-order nonlinearity effects in very high- $Q$  WGM resonator cavity ringdown spectroscopy*, [JOSA B](#) **32**, 370–378 (2015).

## Selbstständigkeitserklärung

Ich erkläre hiermit, dass ich die vorliegende Arbeit selbstständig verfasst und noch nicht für andere Prüfungen eingereicht habe. Sämtliche Quellen einschließlich Internetquellen, die unverändert oder abgewandelt wiedergegeben werden, insbesondere Quellen für Texte, Grafiken, Tabellen und Bilder, sind als solche kenntlich gemacht. Mir ist bekannt, dass bei Verstößen gegen diese Grundsätze ein Verfahren wegen Täuschungsversuchs bzw. Täuschung eingeleitet wird.

Berlin, 22.08.2022

Wang Li